

RIJKSUNIVERSITEIT GRONINGEN

MASTER'S RESEARCH PROJECT
MSc COMPUTATIONAL COGNITIVE SCIENCE

Towards Automatic Classification of Lifetime Visual Hallucinations in Psychosis using Resting-State fMRI

Author:

Helena Luise HAZEU
(s4965671)

Supervisors:
Ashkan NEJAD, M.Sc.
Prof. Frans W. CORNELISSEN

Internal Supervisor:
Dr. Andreea I. SBURLEA

August 1, 2023



Abstract

Although one fourth of patients with schizophrenia experience visual hallucinations, little research has been conducted on the possibility of automated classification of this patient group. Considering the profound detrimental effects associated with the occurrence of visual hallucinations, the identification of classification biomarkers holds great potential for complementing clinical measures, predicting future cases, and guiding personalized treatment of schizophrenia. While several studies have explored the classification of patients with other hallucination modalities, there is a lack of scientific literature on the automated classification of lifetime visual hallucinations. This project aims to classify psychosis patients with and without visual hallucinations using machine learning methods. I implemented an automated pipeline for preprocessing, feature extraction, feature selection by voxel-wise Pearson correlation, and classification of resting-state functional MRI scans. This framework was evaluated on a dataset of 45 psychosis patients and healthy controls. Previous studies demonstrated that alterations in neural activity might predispose patients to schizophrenia and the experience of hallucinations. In line with this research, I assessed five distinct features that are known to capture these alterations: a) regional homogeneity, b) voxel-mirrored homotopic connectivity, c) amplitude of low-frequency fluctuations, d) fractional amplitude of low-frequency fluctuations, and e) eigenvector centrality mapping. A linear support vector machine was employed for classification. The classifier and the features were evaluated based on the classification accuracy on this dataset and the interpretability of the feature weights. By using regional homogeneity, I achieved an accuracy of up to 66.7% when distinguishing individuals with and without visual hallucinations while providing localized regions of high feature importance. For the classification of individuals with visual hallucinations and healthy controls, voxel-mirrored homotopic connectivity led to an accuracy of up to 77.5% and rather localized regions of high feature importance. Lastly, in the classification of subjects with psychosis without visual hallucinations and healthy controls I achieved an accuracy of up to 67.5% by using eigenvector centrality mapping, which yielded dense feature weights that do not indicate localized regions of high significance. I conclude that the trained classifiers are not yet suitable for application in the clinic, while the achieved results are promising. Future research might aim to validate this work on a larger dataset as well as implementing an optimized dimensionality reduction process and investigating the use of more sophisticated artificial intelligence methods.

List of Figures

2.1	Illustration of the number of neighboring voxels K considered for calculation of Regional Homogeneity features. Image from the C-PAC documentation page on Regional Homogeneity [59].	9
2.2	Illustration of homotopic connectivity. VMHC is calculated between voxel A and its mirrored counterpart A' and analogously between B and B'. Figure after [59].	9
2.3	(a) Time-series data from two voxels in the suprasellar cistern (SC) and the posterior cingulate cortex (PCC) of one individual. (b) Power of both voxels. ALFF is the sum of amplitudes between 0.01 and 0.08 Hz. (c) Fractional power for both voxels. fALFF is the sum of amplitudes between 0.01 and 0.08 Hz, divided by the sum of the amplitudes in the total frequency range. Figure from Zou et al. (2008) [67].	11
2.4	Supervised learning. Figure adapted from [75].	13
2.5	Conceptual depiction of a two dimensional linear support vector machine with features x_1 and x_2 . The red and blue datapoints are separated by an optimal hyperplane (black vector), that maximizes the distance between the two support vectors (red and blue dashed lines). A new datapoint is classified based on its location relative to the hyperplane.	15
3.1	Schematic overview of the pipeline that was created in this project.	16
3.2	Age and gender of the participants in the INZICHT2 trial.	17
3.3	Anatomical preprocessing procedure.	20
3.4	Schematic visualization of the cross-validation, feature selection, and classification procedure. The procedure is repeated individually for all five feature types and five times per feature type (5-fold cross-validation). k resembles the feature vector size, which can be set by the user. If k is set to "all", no feature selection is performed and the full feature matrices are used for classification.	22
4.1	Mean performance measures for the classification of PSVH ⁺ vs. PSVH ⁻ .	27
4.2	SVM weights for the classification of PSVH ⁺ vs. PSVH ⁻ using ReHo features with feature selection to 10000 features (top) and ReHo without feature selection (bottom).	28

4.3	SVM weights for the classification of PSVH ⁺ vs. PSVH ⁻ using fastECM features with feature selection to 10000 features (top) and fastECM without feature selection (bottom).	28
4.4	Mean performance measures for the classification of PSVH ⁺ vs. HC.	30
4.5	SVM weights for the classification of PSVH ⁺ vs. HC using VMHC features with feature selection 10000 features (top) and VMHC without feature selection (bottom).	31
4.6	Mean performance measures for the classification of PSVH ⁻ vs. HC.	32
4.7	SVM weights for the classification of PSVH ⁻ vs. HC using fastECM features with feature selection to 1000, 5000, and 10000 features, as well as fastECM features without feature selection (top to bottom).	33
6.1	Median performance measures for the classification of PSVH ⁺ vs. PSVH ⁻ with 95% confidence intervals over five folds.	54
6.2	SVM weights for the classification of PSVH+ vs. PSVH- using ReHo, VMHC, fastECM, ALFF, and fALFF features (top to bottom) without feature selection.	55
6.3	Median performance measures for the classification of PSVH ⁺ vs. HC with 95% confidence intervals over five folds.	56
6.4	SVM weights for the classification of PSVH+ vs. HC using ReHo, VMHC, fastECM, ALFF, and fALFF features (top to bottom) without feature selection.	57
6.5	Median performance measures for the classification of PSVH ⁻ vs. HC with 95% confidence intervals over five folds.	58
6.6	SVM weights for the classification of PSVH- vs. HC using ReHo, VMHC, fastECM, ALFF, and fALFF features (top to bottom) without feature selection.	59

List of Tables

3.1 Demographics and illness characteristics based on van Ommen et al. [4]	18
--	----

List of Abbreviations

ADHD	Attention deficit hyperactivity disorder
AH	Auditory hallucinations
AI	Artificial intelligence
ALFF	Amplitude of low-frequency fluctuations
AUC	Area-under-the-curve
AVH	Auditory verbal hallucinations
BA	Brodmann area
BIDS	Brain imaging data structure
C-PAC	Configurable pipeline for the analysis of connectomes
CI	Confidence interval
CNN	Convolutional neural networks
DCM	Dynamic causal modeling
EC	Eigenvector centrality
ECM	Eigenvector centrality mapping
ELM	Extreme learning machine
EW	Evolutionary wrapper
fALFF	Fractional amplitude of low-frequency fluctuations
FWHM	Full-width at half-maximum
GLM	Generalized-linear model
HC	Healthy control subject group
ICA	Independent component analysis
KCC	Kendall's correlation coefficient
LAAM	Lattice auto-associative memory
LDA	Linear discriminant analysis
LFF	Low-frequency fluctuation
MNI or MNI152	Brain template by the Montreal Neurological Institute
PANSS	Positive and Negative Syndrome Scale
PCA	Principal component analysis
PSVH ⁺	Subject group with psychosis experiencing frequent visual hallucinations
PSVH ⁻	Subject group with psychosis who do not experience visual hallucinations
QPE	Questionnaire for Psychotic Experiences
ReHo	Regional homogeneity
rs-fMRI	Resting-state functional magnetic resonance imaging

rTMS	Repetitive transcranial magnetic stimulation
SBA	Seed-based analysis
SVM	Support-vector machine
V-ELM	Ensemble of extreme learning machines
VH	Visual hallucinations
VMHC	Voxel-mirrored homotopic connectivity

Contents

Abstract	i
1 Introduction	1
1.1 Machine Learning and Psychosis	2
1.2 Classification of Neural Activation Patterns Preceding Hallucinations	4
1.3 Classification of Individuals with Hallucinations	4
1.4 Classification of Individuals with Visual Hallucinations	5
2 Fundamentals	7
2.1 Dimensionality Reduction	8
2.1.1 Regional Homogeneity (ReHo)	8
2.1.2 Voxel-Mirrored Homotopic Connectivity (VMHC)	9
2.1.3 Amplitude of Low Frequency Fluctuations (ALFF) and Fractional Amplitude of Low Frequency Fluctuations (fALFF) .	10
2.1.4 Eigenvector Centrality Mapping (ECM)	11
2.2 Feature Selection	12
2.3 Classification Algorithm	13
3 Methods	16
3.1 Data	17
3.2 Preprocessing	18
3.3 Feature Extraction	20
3.4 Feature Selection	21
3.5 Classification	23
3.6 Evaluation	23
4 Results	26
4.1 Classification of psychosis patients with and without visual hallucinations (PSVH ⁺ vs. PSVH ⁻)	26
4.2 Classification of psychosis patients with visual hallucinations and healthy controls (PSVH ⁺ vs. HC)	29
4.3 Classification of psychosis patients without visual hallucinations and healthy controls (PSVH ⁻ vs. HC)	31
5 Discussion	34

Chapter 1

Introduction

Visual hallucinations pose a remarkable feature of psychiatric disorders such as schizophrenia and schizoaffective disorder. These spontaneous visual perceptions of non-existent objects, animals, people, or textures occur in around 27% of people with schizophrenia, 15% of individuals with schizoaffective disorder, and 7.3% of the general population [1], although estimates vary rather strongly [2]. Typically, individuals on the psychosis spectrum experience visual hallucinations (VH) on top of auditory hallucinations (AH), tactile, gustatory, or olfactory hallucinations [3, 4]. While VH in other physiological diseases, such as Charles Bonnet's syndrome [5, 6], are often benign in character, VH in psychosis are highly complex and negative in content. Additionally, the content of the hallucinations frequently have personal relevance to the person experiencing them [1, 7]. The disease severity of neurodegenerative and psychiatric diseases is also strongly correlated with the occurrence of VH [1]. All of these factors make VH especially debilitating for affected individuals.

The investigation of lasting alterations of the functional connectivity in the brain is especially relevant for assessment and treatment of VH. Resting-state functional magnetic resonance imaging (rs-fMRI) was found to expose these trait-based changes in connectivity [8, 9]. Several studies examined hallucinations using rs-fMRI. Hallucinations in neurodegenerative and psychiatric diseases were linked to excessive influence of higher-order control regions (default-mode and central executive network) over sensory processes [3, 10]. This is supported by several studies finding increased activation of the sensory cortices, such as the visual and auditory cortex, in individuals experiencing hallucinations [11, 12]. In addition, abnormal salience and memory processes, which are modulated by the insula and hippocampus, might also contribute to the experience of hallucinations [3, 13, 14, 15]. Notably, van Ommen et al. [4] found evidence of impaired saliency processing that contributes to wrongful attribution of an external nature to internal visual impulses by using eigenvector centrality mapping (ECM) features. Besides these connectivity analyses, one lesion study found hallucinations to occur following lesions to parts of the cerebellum and the right superior temporal sulcus, pointing to an underlying common network that mediates hallucinations [16].

Artificial intelligence (AI) methods provide new means of analyzing complex data such as MRI and rs-fMRI scans. Compared to traditional statistical analysis, AI methods can be used to find generalizable patterns in the brain for the prediction of future data [17]. These patterns give rise to disease biomarkers that can be employed in early disease detection and inform clinical research [18]. Moreover, AI can be used in the evaluation of treatment effects, prediction of treatment outcomes [19], automatic segmentation [20], and objective assessment of disease to complement other diagnostic tools, such as behavioral assessments [21, 22, 23]. Especially explainable AI algorithms can be beneficial in the medical domain. Thereby the word "explainable" indicates, that the algorithm provides some kind of human-interpretable reasoning on how it arrived at the predictions it makes. This is especially relevant for medical applications, where classification outcomes can have dire consequences. An explainable algorithm can give medical personnel the chance to gain insight into the reasons behind the algorithm outcomes, as well as a point for supervision where they can decide to discard or accept an algorithm outcome based on the reasoning behind it. This is in contrast to the "black box" algorithms, that are not interpretable but have been widely used in the literature as well [24]. Furthermore, the future application of AI methods in neuroimaging holds potential for decoding the content of hallucinations from neural activity [25, 26].

Artificial intelligence techniques are currently employed in a variety of applications in the field of medical imaging and psychiatry for the classification and analysis of rs-fMRI images [22]. While little research has been conducted on the classification of individuals with schizophrenia that experience hallucinations, more studies were conducted on the classification of people with schizophrenia and healthy controls [27, 28].

1.1 Machine Learning and Psychosis

To distinguish people with schizophrenia from healthy controls, features have to be extracted from the rs-fMRI data before feeding the features to a machine learning algorithm. Several feature types have been found useful in classification of schizophrenia in the past. Significant differences in Regional Homogeneity (ReHo), a local measure of connectivity that maps the temporal correlation of a voxel's activity with its neighboring voxels, were found between individuals with schizophrenia and controls [29, 30, 31]. Moreover, schizophrenia has been connected to alterations in inter-hemispheric connectivity, which can be measured using voxel-mirrored homotopic connectivity (VMHC) [32], as well as changes in the strength of low frequency oscillations, measured by amplitude of low-frequency fluctuations (ALFF) and fractional amplitude of low-frequency fluctuations (fALFF) features [33, 34].

Chapter 1. Introduction

For the subsequent classification of schizophrenia, many different machine learning methods yielded good performance at low computation costs in past research [35, 36, 37]. Linear discriminant analysis (LDA) was used in the earlier days of schizophrenia research, while support-vector machine (SVM) methods have been applied more extensively in recent years [27]. Other popular machine learning algorithms for the classification of fMRI images into pathologies are random forests, generalized-linear models (GLMs), the k-nearest neighbors' algorithm, and seed-based analysis (SBA). Moreover unsupervised algorithms such as independent component analysis (ICA), principal component analysis (PCA), and k-means clustering are frequently employed as well. In more recent years, neural network models such as convolutional neural networks (CNNs) gained importance in this field [38, 39].

Two particular studies investigated the automated classification of schizophrenia using one or several of the aforementioned features and classification algorithms: Savio and Graña (2015) [40] and Chyzchyk et al. (2015) [41].

Using a random forest and a support vector machine for the classification of schizophrenia in a large public dataset (COBRE [42]), Savio and Graña [40] achieved a high accuracy while creating an explainable algorithm.

The authors found the highest classification accuracy (up to 80%) for a pipeline using ReHo based local activity features and a random forest for classification. This approach has the advantage of preserving spatial information and subsequently yielding a set of voxels that has the highest predictive power. With this, the authors were able to retrieve the most distinct features of schizophrenia in the brain as biomarkers that can be used in subsequent classifications.

Chyzchyk et al. [41] sought to discriminate between subjects with schizophrenia and healthy controls by using a more computationally efficient method. They employed an ensemble of extreme learning machines (V-ELMs) for classification. Several functional activity measures served as features to be used as input to the classifier. These were ALFF and fALFF, VMHC, as well as ReHo. The most useful features were selected using an evolutionary wrapper (EW) algorithm on Pearson's correlation maps of the functional activity features.

The V-ELM achieved an accuracy of around 90% (on the VMHC features) in the classification of the COBRE dataset in a short computation time and with conventional resources. This approach is also explainable by providing voxel-size locations of the most discriminant features by visualizing the selected voxel clusters of the Pearson's correlation map.

1.2 Classification of Neural Activation Patterns Preceding Hallucinations

While the above-mentioned papers investigated alterations of the connectome [43] in schizophrenia, machine learning has also been applied to the classification of individuals with hallucinations. Thereby, AH have been investigated more frequently than visual hallucinations [28, 44]. This is likely due to VH occurring only half as often as AH in psychosis [45]. Moreover, VH often co-occur with AH, making it difficult to disentangle the neural correlates of VH and AH for a high classification performance [13].

Fovet et al. [46] investigated the use of a linear SVM classifier to decode activity in the brain, especially in Broca's area, that precedes auditory verbal hallucinations (AVH). The classifier yielded an area-under-the-curve (AUC) value of 0.85 in the discrimination of periods of AVH from resting periods and task-based activity during a verbal imaginary task. The authors also built contribution maps that showed a strong contribution of brain regions previously associated with the pathophysiology of AVH (e.g. Broca's area and the supplementary motor area).

De Pierrefeu et al. [44] investigated the use of an SVM-based algorithm and a regularized logistic regression classifier (TV-Enet) to identify brain states in rs-fMRI scans of individuals with schizophrenia that precede any modality of hallucinations. The classifiers achieved AUC values of 0.73 and 0.79 for the SVM and TV-Enet classifiers, respectively.

To make the classification results more interpretable, the authors also constructed predictive weight maps for both classifiers. The most salient networks in the prediction of imminent hallucinations were speech-related areas, that were previously found to be involved in AVH [47], such as Broca's area. Conversely, areas associated with other hallucination modalities (such as the visual cortex), did not account for much of the predictive power of the classifier. This is likely due to the small number of participants experiencing VH compared to the large number of people with AVH in their dataset. Hence, this classifier is possibly less suitable for the prediction of imminent visual hallucinations, compared with its good performance in predicting AVH.

1.3 Classification of Individuals with Hallucinations

The classification of people with hallucinations using machine learning methods has been investigated in the literature as well. In comparison to predicting imminent hallucinations, classifying lifetime hallucinations involves the detection of trait-associated connectivity alterations that exist irrespective of the individual's experience of hallucinations at scanning time. Thereby, lasting changes in the connectome are more relevant than short-term changes in neural activity.

Chapter 1. Introduction

Graña et al. [48] used dynamic causal modeling (DCM) and an SVM classifier to determine if participants are likely to experience lifetime AH based on the effective connectivity between brain regions in their rs-fMRI scans. This approach has the advantage of using causality as the discriminant feature, which provides a new perspective on AH.

The same task was investigated by Chyzhyk et al. [28]. The authors compared functional connectivity measures, such as lattice auto-associative memories (LAAM), and local activity measures, such as ALFF, fALFF, and ReHo. Subsequently, they created an SVM-based classifier that is able to distinguish individuals that experience AH and suffer from schizophrenia from those that do not, and healthy controls, with an accuracy of up to 100%.

Schutte et al. [3] investigated the differences in connectivity of people with psychosis and bipolar I disorder, as well as non-clinical individuals, with auditory and visual hallucinations. Using a random forest classifier, they were able to distinguish non-clinical individuals with only AH from those with both AH and VH with an accuracy of 77.5%, a specificity of 93.9% and a sensitivity of 0%. Distinguishing participants with schizophrenia with AH and VH and from those with only VH yielded an accuracy of 50% (chance level). The same classification for individuals with bipolar I was also not possible (28.6% accuracy, below chance level). One reason for these partly insignificant results might be, that the participants in this study experienced several hallucination modalities at a time. This makes discrimination between the groups more difficult [3].

1.4 Classification of Individuals with Visual Hallucinations

While VH in physiological disorders were investigated more thoroughly, research in the field of VH in psychosis is rather sparse [1, 3, 13]. Several studies on the automated classification of schizophrenia [41, 49, 50] and AH [28, 46, 51] in rs-fMRI scans have been conducted. However, only a very limited number of studies included participants with VH [3, 44] and no study was successful in classifying lifetime VH in participants with psychosis using machine learning. Investigations into neuroimaging biomarkers of VH can inform further research on this topic and possibly complement clinical diagnosis procedures for VH in the future.

Considering the absence of AI-driven studies addressing VH classification in the existing literature, the aim of this project is to develop a reusable machine learning pipeline for the purpose of classifying lifetime VH in rs-fMRI images of individuals with psychosis. Based on previous research on other hallucination modalities [3, 4, 28, 41], several feature extraction methods and classifiers were investigated. Specifically, I assessed ReHo, ALFF, fALFF, VMHC, and ECM

Chapter 1. Introduction

features. This selection was made based on previous work that showed good correspondence between these features and the physiopathology of hallucinations and schizophrenia [4, 30, 32, 33, 34].

A linear SVM was utilized for classification in line with previous research on auditory hallucinations and schizophrenia [28, 44, 46], where this classifier yielded good results. To increase the algorithm's explainability and the clinical applicability of the obtained results, I compared the features with respect to the classification accuracy, as well as the visual interpretability of the feature weights.

The main contributions of this project are:

- Creating an automated and reusable pipeline for preprocessing, feature extraction, feature selection, classification, and analysis of rs-fMRI images.
- Testing the pipeline on a dataset comprised of 45 individuals with schizophrenia and healthy controls.
- Assessing five feature extraction methods for detection of lifetime VH, considering classification accuracy as well as interpretability of the feature weights.

The following report can be divided into five main sections. Firstly, I provide a theoretical explanation of the used methods and algorithms in Section 2. Secondly, the data and the concrete implementation of the algorithms in Python are detailed in Section 3. Afterwards, the results will be presented and discussed (Section 4 and 5). Lastly, I provide an outlook for possible future work in the final section of this report (Section 6).

The code to this project is publicly available on GitHub¹.

¹https://github.com/LEO-UMCG/Visual_Hallucinations_Classification

Chapter 2

Fundamentals

A pipeline for the classification of high-dimensional data typically encompasses several steps [39].

Raw fMRI images often suffer from a low signal-to-noise ratio as well as bad alignment of the brain within the scans. Therefore, the raw fMRI images should be preprocessed first to convert all images into the same space, reduce noise, and normalize the intensities to allow for improved feature extraction later.

Once the images are preprocessed, the data has to be reduced to increase the computational efficiency of the algorithm and also extract the most important features from the fMRI data. Thereby, several different features can be extracted in order to distill different kinds of structures and relationships from the data. What results is a 3D image, that represents the functional and temporal relationships in the 4D fMRI scan.

Following the feature extraction step, feature selection can also be performed. Methods of feature selection are widely used in the literature and contribute to a more efficient and effective pipeline [28, 40]. By selecting the most relevant features from the data, the classification algorithm can perform in an optimal manner and at a lower computational cost. Moreover, feature selection can improve the generalizability of the algorithm by reducing noise components and condensing the input to the most relevant information.

After feature selection, one optimally obtains a set of data that contains the most important information with the least amount of noise possible. This data is then used to train a classification algorithm, which ideally would be able to predict future cases with a high accuracy.

Details about each of the aforementioned steps and how they were incorporated in the pipeline for this project will be presented in the following sections.

2.1 Dimensionality Reduction

Functional MRI scans are acquired by conducting many scans over a period of typically a few minutes. The resulting fMRI image has three spatial dimensions and one time dimension. The spatial dimensions are represented by voxels, values in 3D space that are analogous to a pixel in 2D space. This four dimensional representation of the brain yields a large amount of data for each participant.

Therefore, the data has to be reduced into a three dimensional image with scalar values for each voxel for subsequent classification. Feature extraction methods allow for the extraction of different quantifications of functional connectivity within the brain into scalar values.

In this project, I compared five different local activity measures, which will be described in the following subsections.

2.1.1 Regional Homogeneity (ReHo)

ReHo is a measure of the similarity of activity over time within a cluster of voxels [52]. Significant changes in ReHo were found in studies studying bilateral finger movements [52], individuals with attention deficit hyperactivity disorder (ADHD) [53, 54], and subjects with schizophrenia [55, 56, 57].

Moreover, one study used ReHo features to classify people with schizophrenia and auditory hallucinations with a high accuracy [28].

To create a ReHo representation of an fMRI scan, each voxel gets assigned a Kendall's correlation coefficient (KCC) [58] that is calculated by determining the KCC of this voxel's time series and those of its neighboring voxels as follows:

$$W_j = \frac{\sum_i (R_i)^2 - n(\bar{R})^2}{\frac{1}{12} K^2 (n^3 - n)}. \quad (2.1)$$

Here, $W \in [0, 1]$ is the KCC, with high values representing a high similarity between voxel activations of neighboring voxels. n is the number of ranks [52]. $R_i = \sum_{k=1}^K r_{ik}$ is the sum of the ranks of the k voxels in the cluster at timepoint i and $\bar{R} = ((n+1)K)/2$ is the mean of the R_i 's, where K is the cluster size. Several cluster sizes can be chosen, some of which are depicted in Figure 2.1.

In this project, I calculated ReHo as the correlation between a voxel and its 26 neighbors on the faces, edges, and corners ($K = 27$) in accordance with Chyzhchuk et al. (2015) [28]. This results in a cube-shaped 3D cluster around each considered voxel (3mm x 3mm x 3mm). The output is a scalar value for each voxel j that represents this voxel's coactivation with its neighborhood over the scanning period.

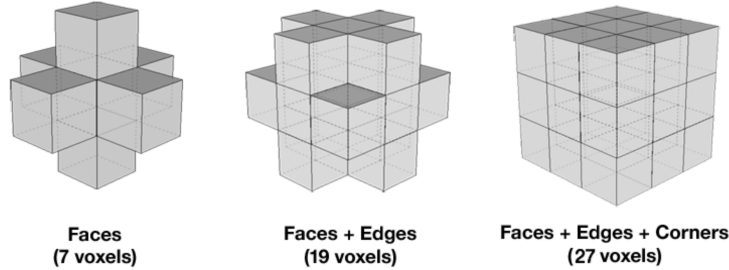


Figure 2.1: Illustration of the number of neighboring voxels K considered for calculation of Regional Homogeneity features. Image from the C-PAC documentation page on Regional Homogeneity [59].

2.1.2 Voxel-Mirrored Homotopic Connectivity (VMHC)

Being a largely symmetric and, simultaneously, complex and interconnected organ, the brain is composed of two nearly mirrored hemispheres. Many functions arise through a cooperation of areas in both hemispheres, while some are controlled unilaterally. Examples for unilateral control are the comprehension and articulation of spoken language, which are controlled mainly by Wernicke's and Broca's area on the left side of the brain, respectively [60].

Thus, measuring the synchrony of activity of one voxel site, with its mirrored counterpart on the other hemisphere can lend itself for the study of tasks that involve unilateral control, such as motor control or speech [61]. Moreover, some diseases that are characterized by differences in interhemispheric connectivity, such as schizophrenia and the experience of hallucinations, can also be investigated by measuring this functional homotopy [32, 62].

One such measure for assessing interhemispheric connectivity is VMHC [61]. It is a quantification of voxel-wise resting state functional connectivity between the hemispheres [63, 64]. VMHC is calculated by measuring the functional connectivity of each voxel with its geometrically mirrored counterpart in the other hemisphere. This homotopic connectivity is depicted in Figure 2.2.

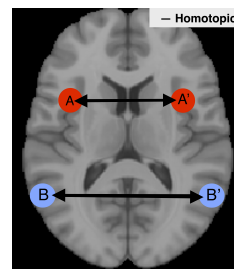


Figure 2.2: Illustration of homotopic connectivity. VMHC is calculated between voxel A and its mirrored counterpart A' and analogously between B and B'. Figure after [59].

2.1.3 Amplitude of Low Frequency Fluctuations (ALFF) and Fractional Amplitude of Low Frequency Fluctuations (fALFF)

ALFF provides a measure of regional synchrony of activity in the brain by measuring regional spontaneous low-frequency ($f < 0.08\text{Hz}$) fluctuations (LFF) in rs-fMRI images [65]. This regional synchrony was found to be decreased in individuals with ADHD [54, 65] and schizophrenia [33] compared with healthy control subjects, suggesting that a global disconnect within the brain might be underlying these diseases.

ALFF is extracted by linear detrending of the time-series data, determining the power spectra using Fast Fourier Transform, and calculating the averaged square root of all frequencies between 0.01 and 0.08Hz (low frequency range) for this voxel. This means, that ALFF is the sum of all amplitudes in the low frequency range for one voxel.

The formula [66] for obtaining the ALFF for a voxel j , with f being the frequency, is thus:

$$ALFF_j = \sum_{f=0.01}^{0.08} A_f. \quad (2.2)$$

Zou et al. improved ALFF by reducing its sensibility to physiological noise by proposing the fractional ALFF measure (fALFF) [67]. Changes in fALFF were found in individuals with schizophrenia as well [33].

The fALFF for one voxel j is computed by dividing the sum of amplitudes in $[0.01, 0.08\text{Hz}]$ (Equation 2.2) by the sum of amplitudes across the total frequency range in the image as follows:

$$fALFF_j = \frac{\sum_{f=0.01}^{0.08} A_f}{\sum_{f=0}^{N-1} A_f}, \quad (2.3)$$

with f being the frequency and N being the maximum frequency in the time series (Nyquist frequency) [66].

Figure 2.3 depicts the intensity time-series of two voxels, and how the power and fractional power can be used to determine ALFF and fALFF.

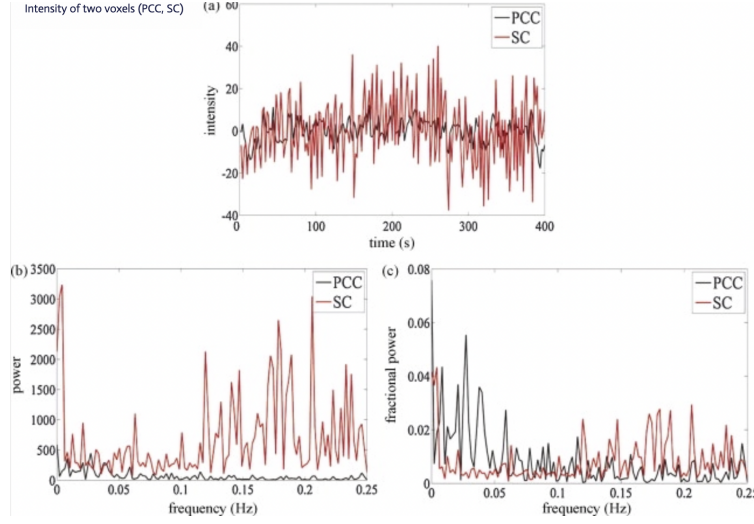


Figure 2.3: (a) Time-series data from two voxels in the suprasellar cistern (SC) and the posterior cingulate cortex (PCC) of one individual. (b) Power of both voxels. ALFF is the sum of amplitudes between 0.01 and 0.08 Hz. (c) Fractional power for both voxels. fALFF is the sum of amplitudes between 0.01 and 0.08 Hz, divided by the sum of the amplitudes in the total frequency range. Figure from Zou et al. (2008) [67].

2.1.4 Eigenvector Centrality Mapping (ECM)

The centrality of a component of a brain network, a node, is a representation of the amount of exchange of information this node has with other nodes in the network [68]. Nodes with high centrality are, therefore, hubs with high connectivity to many other nodes, that also have ah a high centrality. This centrality can be represented by voxel-wise eigenvector centrality (EC) [69], but also by other centrality types such as between or degree centrality [70].

Eigenvector centrality mapping was found to represent changes in the functional connectome of the brain in people with Alzheimer's disease [71]. Moreover, a study from my group by van Ommen et al. [4] found significant changes in ECM for subjects with schizophrenia and VH. ECM might also be useful in individual treatment of VH using high-frequency repetitive transcranial magnetic stimulation (rTMS), as a case study by Invernizzi et al. [72] showed. Using ECM, network hubs can be identified and used as targets for precision treatment if they differ strongly between control subjects and individuals experiencing VH.

The EC of a voxel is the coefficient in the eigenvector with the largest eigenvalue in the connectivity matrix. Thus, the EC is the sum of centralities of the voxels close to the considered voxel [68].

Wink et al. [70] created a computationally efficient version of the ECM algorithm, the fastECM method, which will be used to calculate the ECM feature map in this

project. In fastECM, the product of the connectivity matrix with the estimate of the eigenvector is computed at each iteration. This saves computation time and memory consumption by making the explicit storage of the connectivity matrix obsolete.

2.2 Feature Selection

The local activity measures that were computed provide a 3D representation of the connectivity in the brain. The size of the feature maps depends on both the resolution (voxel size) and the size of the brain. As an example, a ReHo map in this study is a three-dimensional matrix with 271633 scalar entries with shape (61, 73, 61), whereby each entry is the ReHo of this specific voxel. This can be envisaged as a cube with 61 rows, 73 columns, and 61 slices along the three axes.

Given the high dimensionality of the feature maps, further feature selection is useful to extract the most relevant features and discard of less relevant ones. Moreover, feature selection improves the subsequent classification outcomes by increasing the signal-to-noise ratio of the input.

In this project, I conducted feature selection by Pearson's correlation on the previously computed feature maps in concordance with previous studies in the field of hallucinations and schizophrenia detection [28, 40, 41].

Pearson's correlation [73, 74] is a measure of the linear correlation between two variables \mathbf{x} and \mathbf{y} . The Pearson's correlation coefficient ($r \in [-1, 1]$) is defined as the covariance of variables \mathbf{x} and \mathbf{y} divided by their standard deviations. In the present study, I determine the voxel-wise Pearson correlation.

The voxel-wise Pearson's correlation coefficient r_j for a voxel j is then computed as follows:

$$r_j(\mathbf{x}_j, \mathbf{y}) = \frac{\sum_{i=1}^N (x_{i(j)} - \bar{x})(y_i - \bar{y})}{\sqrt{\sum_{i=1}^N (x_{i(j)} - \bar{x})^2} \sqrt{\sum_{i=1}^N (y_i - \bar{y})^2}}, \quad (2.4)$$

where \mathbf{x}_j is the vector of each subject's activity value for one voxel j . The Pearson's coefficient r_j is calculated for each voxel individually by taking the intensity of the feature map in one voxel location for every training subject N into account. \bar{x} and \bar{y} are thereby the mean of \mathbf{x}_j and \mathbf{y} respectively.

A Pearson r coefficient of 1 represents a perfect positive correlation, while $r = 0$ represents no correlation. $r = -1$ represents a perfect negative correlation between the variables. In this work, the Pearson r value is used as a saliency measure to select the most discriminative voxels. Voxel sites with r close to 0 are not informative or discriminative for distinction between the two classes and can be discarded.

The voxel sites with the highest or lowest r values represent the most informative voxels for classification. The full feature selection procedure is further outlined in Section 3.4.

2.3 Classification Algorithm

In classification of lifetime VH in this work, a supervised machine learning problem is solved. The input data is comprised of a dataset of rs-fMRI images, as well as corresponding subject labels that were determined by a trained clinician. Supervised machine learning aims to train an algorithm on a dataset that was labelled by a medical professional. Features that differentiate the considered groups are subsequently identified during training. Afterwards, the algorithm can classify unlabelled data using these features to assist in diagnosis. An outline of a supervised learning problem is depicted in Figure 2.4.

As a supervised machine learning method with manifold options for application and ease of use, SVMs gained large popularity in many fields of research. This efficient algorithm for the minimization of the cost function was first proposed by Vapnik and Chervonenkis [76] and improved by Boser et al. [77]. The main advantages of SVMs are their computational efficiency, reproducibility, explainability, and high performance, even on small training datasets (below a few hundred participants) [78].

SVMs are a method of supervised machine learning, whereby a set of n -dimensional features \mathbf{x}_i and corresponding training labels $y_i \in \{1, -1\}$ are used to learn a hyperplane that best separates the two classes. This hyperplane is constructed to achieve a maximum margin between each class and the hyperplane.

The hyperplane of a linear SVM is computed by considering the support vectors for each class label. These vectors lie on those two datapoints, that are the closest to the respective other class (see Figure 2.5 in red and blue). The hyperplane then lies in the middle of these two support vectors and is parallel to them. Thereafter, each new, unseen datapoint can be classified as belonging to either class, based on its location relative to the hyperplane.

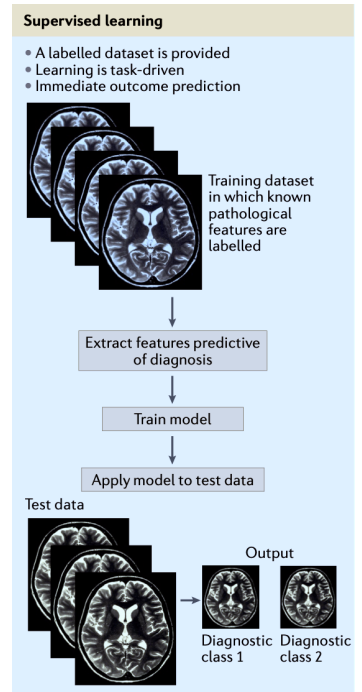


Figure 2.4: Supervised learning. Figure adapted from [75].

Mathematically a linear SVM minimizes the following equation:

$$C\|\mathbf{w}\|^2 + \left[\frac{1}{N} \sum_{i=1}^N \max \left(0, 1 - y_i(\mathbf{w}^\top \mathbf{x}_i - b) \right) \right], \quad (2.5)$$

where \mathbf{w} is the normal vector to the SVM that represents the weights of the classifier, N is the number of datapoints, and C is a regularization parameter. $\frac{b}{\|\mathbf{w}\|}$ is the offset of the hyperplane from the intercept in the direction of \mathbf{w} (gray line in Figure 2.5). The ultimate goal is to maximize the margin $\frac{2}{\|\mathbf{w}\|}$.

The hyperplane can be described by

$$\mathbf{w}^\top \mathbf{x} - b = 0, \quad (2.6)$$

and each support vector is described by

$$\mathbf{w}^\top \mathbf{x} - b = \begin{cases} 1 & \text{positive class} \\ -1 & \text{negative class} \end{cases}. \quad (2.7)$$

All datapoints are therefore constrained to the following equations:

$$\mathbf{w}^\top \mathbf{x}_i - b \geq 1, \text{ if } y_i = 1 \quad (2.8)$$

or

$$\mathbf{w}^\top \mathbf{x}_i - b \leq -1, \text{ if } y_i = -1, \quad (2.9)$$

which make sure that all datapoints lie on the correct side of the hyperplane.

The hyperparameter C allows for a certain amount of datapoints to fall into or out of the margin to build a more generalizable classifier and prevent overfitting. An SVM that uses a regularization parameter C is called a "soft-margin" SVM. The amount of allowed misclassifications is thereby proportional to C .

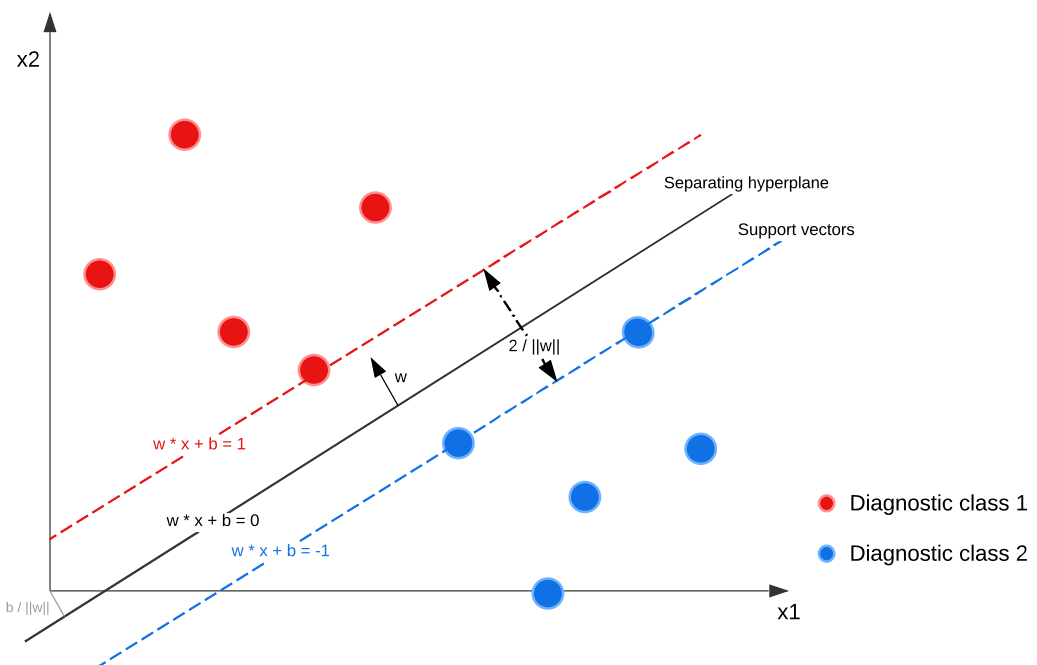


Figure 2.5: Conceptual depiction of a two dimensional linear support vector machine with features x_1 and x_2 . The red and blue datapoints are separated by an optimal hyperplane (black vector), that maximizes the distance between the two support vectors (red and blue dashed lines). A new datapoint is classified based on its location relative to the hyperplane.

Chapter 3

Methods

In the following sections, I explain each step of the pipeline for the classification of individuals with visual hallucinations and present the dataset. I used a dataset from a group of 45 individuals with psychosis and healthy controls. The data was then preprocessed to increase the signal-to-noise ratio of the rs-fMRI scans. Then, I extracted five different features to compare their performance. After a feature selection step, the features are supplied to a linear SVM classifier.

Figure 3.1 illustrates the designed pipeline in this project. All parts of the pipeline were implemented in Python except for the fastECM feature extraction step. I outline the specification of each step in the sections below.

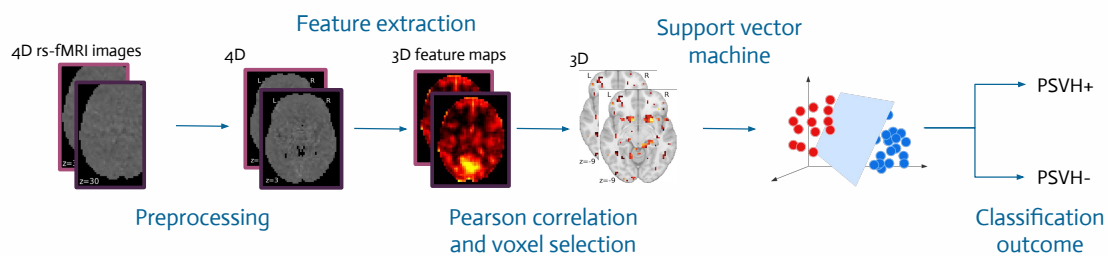


Figure 3.1: Schematic overview of the pipeline that was created in this project.

3.1 Data

The dataset used for training and testing the pipeline in this project was collected by van Ommen et al. [4] as part of the INZICHT2 trial. It is comprised of 45 individuals in total, including subjects diagnosed with schizophrenia ($n = 16$), schizoaffective disorder ($n = 6$), psychotic disorder: not otherwise specified (NOS; $n = 7$), as well as healthy controls ($n = 16$). Table 3.1 summarizes the characteristics of the participants in the INZICHT2 trial. A visualization of the age and gender characteristics can also be seen in Figure 3.2.

The participants were assembled into three groups based on the frequency and characteristics of their hallucinations: 1) Those subjects with psychosis experiencing frequent visual hallucinations (PSVH⁺; $n = 14$), 2) subjects with psychosis who do not experience visual hallucinations (PSVH⁻; $n = 15$), and 3) healthy controls (HC; $n = 16$). The severity of hallucinations was assessed with the Positive and Negative Syndrome Scale (PANSS) [79] and the Questionnaire for Psychotic Experiences (QPE) [80].

Notably, all subjects with psychosis participating in the study experienced some form of hallucinations, such as auditory or olfactory hallucinations. The PSVH⁻ group reported experiencing other hallucination modalities, such as auditory or tactile hallucinations, but no visual hallucinations. The PSVH⁺ group, on the other hand, experienced frequent VH on top of other hallucination modalities.

The fMRI scans were acquired at the Neuroimaging Center in Groningen. The scanning time amounted to 10 minutes, during which participants were instructed to remain in a relaxed but awake state with their eyes closed. Functional images (TR 2s, TE 30ms, 3mm voxel size, flip angle 90°, 39 slices per volume) and T1 weighted scans (1mm voxel size, 160 slices) were collected with a 3T Philips scanner. After the scanning procedure was finished, participants were interviewed about any hallucinations they might have experienced while in the scanner. Three individuals

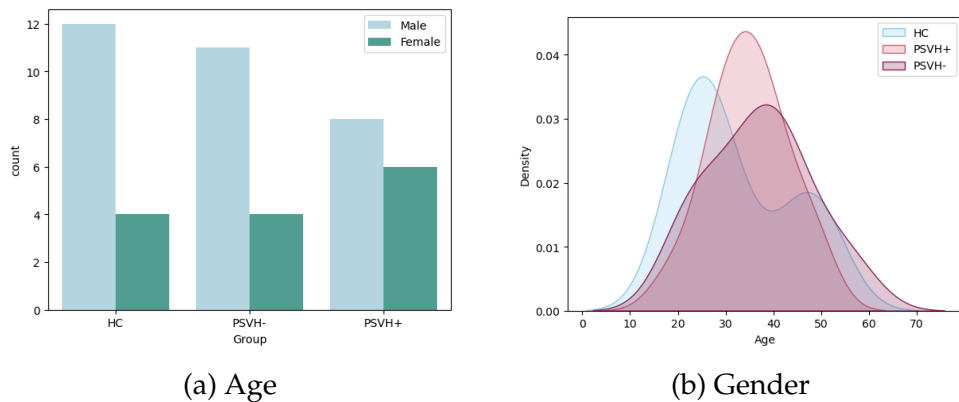


Figure 3.2: Age and gender of the participants in the INZICHT2 trial.

Chapter 3. Methods

Table 3.1: Demographics and illness characteristics based on van Ommen et al. [4]

	PSVH+	PSVH-	HC
Age (mean y, SD)	34.9 (8.1)	34.9 (8.1)	32.4 (11.2)
Gender (n, %)			
Male	8 (57.1)	12 (80.0)	12 (75.0)
Female	6 (42.9)	3 (20.0)	4 (25.0)
Diagnosis (mean, SD)			
Schizophrenia	7 (50.0)	9 (60.0)	
Schizoaffective disorder	2 (14.3)	4 (26.7)	
Psychosis NOS	5 (35.7)	2 (13.3)	
Disease duration (mean y, SD)	11.1 (9.0)	15.1 (12.6)	
PANSS (mean, SD)			
tot pos	19.3 (4.5)	14.3 (5.2)	7.6 (0.7)
tot neg	16.0 (5.9)	13.9 (3.4)	7.9 (1.6)
tot gen	38.4 (8.8)	31.7 (8.0)	18.3 (1.5)
tot	73.7 (16.6)	59.8 (14.9)	33.8 (2.4)
QPE+ (mean, SD)			
severity VH	11.9 (4.4)	0 (0)	
severity AH	13.1 (11.2)	6.2 (9.7)	
severity all H	26.7 (13.2)	6.8 (10.6)	
severity delusions	5.2 (5.8)	4.6 (5.4)	

in the PSVH⁻ group and seven subjects in the PSVH⁺ group experienced hallucinations at scanning time. For more details on the procedure and the participants, please consult the paper by van Ommen et al. [4].

3.2 Preprocessing

Before further analyses were conducted, I preprocessed the rs-fMRI images and the T1w anatomical scans. I conducted all preprocessing steps for each subject individually and the steps and settings for the pipeline configuration were the same to allow for between-subject comparisons.

Before preprocessing the images, they were converted from DICOM to the widely used Nifti [81] format using dcm2nii [82]. Moreover, the images were arranged to the Brain Imaging Data Structure (BIDS) [83, 84] format for compatibility with the subsequent processing steps.

I used the Configurable Pipeline for the Analysis of Connectomes (C-PAC) [85] to preprocess all images. This open-source and easy-to-use pipeline is a combination of other popular preprocessing packages such as FSL [86], Freesurfer [87], and AFNI [88, 89].

To make the comparisons between this study and other papers easier, this pipeline has been validated and widely used in the literature [40, 41, 90]. Moreover, using a fully automated pipeline for preprocessing makes this work more reproducible.

Chapter 3. Methods

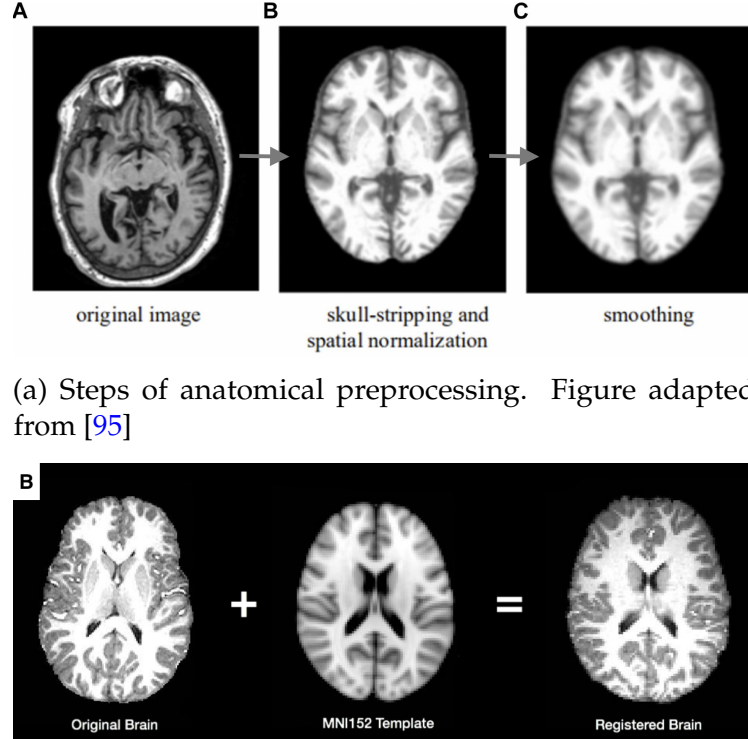
The configuration file that was used was supplied in the GitHub repository of this project¹. All preprocessing steps that are detailed below run fully automated by running a C-PAC singularity container. This C-PAC singularity container is a software component that contains all necessary packages and files to easily use C-PAC with one terminal command and that can be run on high performance cluster computers. More information can be found on the C-PAC website [59].

Anatomical preprocessing with C-PAC begins with resampling of the brain volume to the Montreal Neurological Institute (MNI152) brain template [91] with a resolution of 2mm using FSL. Then, the brain volume is extracted from the image and smoothed with AFNI 3dSkullStrip. Subsequently, tissue segmentation into white matter, gray matter, and cerebrospinal fluid is performed with FSL-FAST [92]. An overview of the anatomical preprocessing steps can be seen in Figure 3.3a and the process of alignment to the MNI152 template is visualized in Figure 3.3b.

No fMRI volumes were discarded since scanner calibration was performed before the scans were recorded.

Functional preprocessing started by slice timing correction and motion correction (AFNI 3dvolreg [93]). Next, the functional images are transformed to MNI152 space using FSL. Then, nuisance regression is performed by regressing out white matter and cerebrospinal fluid components, and performing first principal component removal using a 24-regressor model of motion [94]. The scan is bandpass filtered between 0.001Hz and 0.1Hz, spatially smoothed using a 4mm full-width at half-maximum (FWHM) kernel, z-scored, and written to 3mm MNI space.

¹https://github.com/LEO-UMCG/Visual_Hallucinations_Classification.git



(b) Spatial normalization to MNI152 template (step B). Figure adapted from [59]

Figure 3.3: Anatomical preprocessing procedure.

3.3 Feature Extraction

After preprocessing, five different voxel-wise connectivity analyses are performed on the functional scans, namely ReHo, VMHC, ALFF, fALFF, and fastECM. I apply each feature extraction method to the preprocessed functional MRI scan of each subject individually, yielding five feature maps per subject.

I extract the first four feature maps (ReHo, VMHC, ALFF, and fALFF) using the C-PAC pipeline. This also runs fully automated when starting the C-PAC singularity container. The last feature map type (voxel-wise ECM) was extracted using the computationally efficient fastECM method by Wink et al. [70].

Below, the steps for computing the ReHo, VMHC, ALFF, fALFF, and fastECM features are outlined (information based on [59] and [70]).

- **ReHo:** ReHo is calculated in original space where the simultaneous Kendalls correlation is determined between the time course of each voxel and the time courses of all 27 neighboring voxels (face, edge, and corner). The image is written to 3mm original space and z-scored afterwards.
- **VMHC:** The anatomical scan is first transformed to a symmetric brain template at 2mm resolution. Then, the functional scan is normalized to this

symmetric anatomical image. VMHC calculates the correlation between voxels and their corresponding voxel in the other hemisphere. The resulting values are Fisher transformed, spatially smoothed (6mm FWHM) and written to symmetric space at 2mm.

- **ALFF:** After bandpass filtering ($0.001\text{Hz} < f < 0.1\text{Hz}$) in original space, the variance of each voxel is calculated and written to MNI space (3mm resolution). Afterwards, the image is spatially smoothed with a 6mm FWHM gaussian kernel and z-scored.
- **fALFF:** The same process as for ALFF is conducted but the signal variance is divided by the total variance of the non-bandpassed signal.
- **fastECM:** I imported the cleaned and MNI aligned functional scans (3mm resolution) manually into the MATLAB GUI provided by Wink et al. (GitHub repository: [96]) along with a 3mm MNI mask (retrieved from [97]). The ReLU option for the connectiviy calculation was selected to extract a real-valued ECM map.

Firstly, the MNI mask is applied to discard of any remaining voxels outside of the MNI brain volume. The similarity between voxels is determined by calculating the correlation between the time courses of each voxel pair. The fastECM algorithm thereby computes the product with the eigenvector estimate at each iteration instead of saving the complete connectivity matrix. The resulting matrix is written to MNI space at a resolution of 3mm.

Figure 3.4 shows the further process after feature extraction. Once the nifti images of each feature type (five feature maps per subject) are saved in memory, the process starts with the block at the top (for instance "N ReHo maps"). I run the same process for all five feature types. This yields model performance measures for each combination of feature type and feature vector size. The steps shown in Figure 3.4 are discussed thoroughly in the following sections.

3.4 Feature Selection

In order to extract the most salient features from the high-dimensional feature matrices, improve the signal-to-noise ratio and reduce the computational complexity, I perform feature selection by voxel-wise Pearson correlation individually for each feature map type.

All input images are first masked to the MNI152 template to discard of any remaining voxels outside of the MNI volume. The ReHo, ALFF, fALFF, and fastECM images are masked with an MNI mask at a resolution of 3mm [97]. The VMHC images are masked with a 2mm MNI mask [98]. After reading in one feature map for each of the subjects, I use a fully independent five-fold cross-validation procedure to split the dataset into train and test sets of 80% and 20%, respectively. The feature selection and classification are performed for each fold separately. This

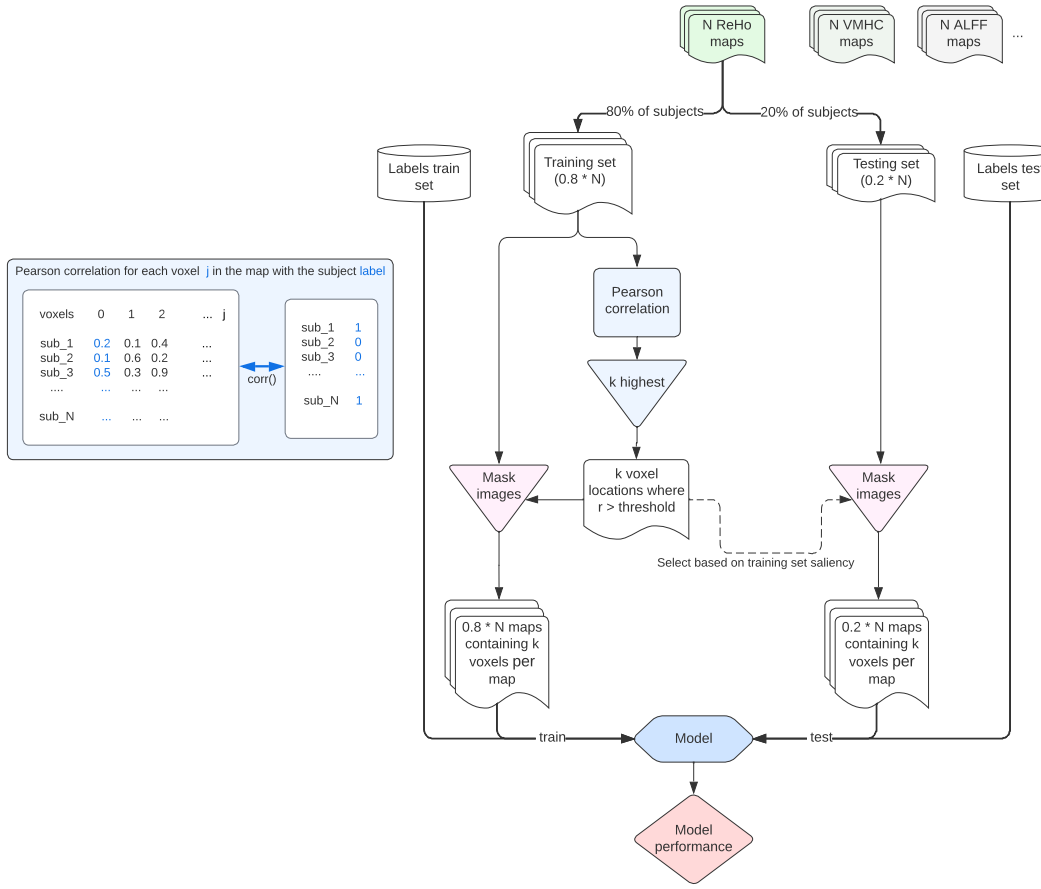


Figure 3.4: Schematic visualization of the cross-validation, feature selection, and classification procedure. The procedure is repeated individually for all five feature types and five times per feature type (5-fold cross-validation). k resembles the feature vector size, which can be set by the user. If k is set to "all", no feature selection is performed and the full feature matrices are used for classification.

ensures, that no information from the testing set contributes to the training of the classifier. I used the `sklearn.model_selection.StratifiedKFold()` method by Scikit-learn which takes the subject labels into account to ensure balanced labels in the train and test sets. To perform Pearson correlation, the class labels were converted to either a 1 (positive label) or 0 (control label).

Afterwards, my pipeline computes the Pearson correlation between one voxel's intensity for all feature maps of the training set with the corresponding subject labels. This is done for every voxel in the 3D feature map (blue box in Figure 3.4). The result is a 3D map with the same dimensions as the input matrix, that contains one Pearson r_j value for each voxel location (Equation 2.4), thereby representing its saliency for distinguishing the two classes.

For generating a feature selection mask, the absolute Pearson r values are sorted and the k th highest ranking value is determined. k is the desired feature vector size, to which the matrix should be reduced. This value can be set by the user as a hyperparameter. All voxels with a Pearson correlation coefficient below the k th strongest absolute correlation value are discarded of, while the other voxels remain with a value of 1. The resulting selection mask is applied to all N feature maps of the considered feature map type (training and testing set). Afterwards, each subject's feature map only contains the k most salient voxels.

I chose to test four different feature vector sizes in this study, including 1000, 5000, 10000, and "all". The option "all" indicates, that all features were used for classification and that no feature selection was performed. The feature vector sizes were chosen based on previous work by Chyzchyk et al. [28].

3.5 Classification

I performed classification of the feature maps into pathologies using the popular Nilearn [99] and Scikit-learn [100] Python analysis packages.

After feature selection, matrices for each combination of feature type and feature vector size for every participant are present in memory (e.g. ReHo with $k = 1000$, fECM with $k = 5000$, etc.). To optimally exploit the performance of the SVM in classification, I first scale the matrices to zero mean and unit variance using the `sklearn.preprocessing.StandardScaler()` function. The scaler is first fitted to the train set and subsequently used to transform both the train and test set. Then, I conducted the classification of the images using a linear SVM (`sklearn.svm.LinearSVC()` method). A list of matrices, as well as the corresponding subject labels, is supplied to the linear SVM classifier. In each fold, the feature selection and classification procedure is performed on the train and test sets as described before. This yields an average test accuracy, sensitivity, and specificity over five folds.

3.6 Evaluation

In this section, I evaluate the performance of the pipeline in three separate experiments. Firstly, the classification of PSVH⁺ and PSVH⁻ will be evaluated. In distinguishing individuals with psychosis and VH from those without VH, I aim to identify biomarkers specific to the experience of VH. Secondly, I classify PSVH⁺ and HC. This classification experiment aims to identify connectome differences between individuals with psychosis that experience VH on top of other hallucination modalities and healthy control subjects that experience neither symptoms of psychosis nor hallucinations. Since the functional connectivity of individuals with severe psychosis was found to differ strongly from individuals without psychosis (Section 1), the classifier will likely find differences not only related to VH but other dimensions of psychosis as well. Finally, I classify PSVH⁻ and HC. This experiment serves as a baseline for interpretation of the results of PSVH⁺ vs. HC

Chapter 3. Methods

to disentangle the algorithms capacity to classify VH from its ability to classify markers of psychosis in the brain.

The performance of the classifier is measured based on the number of correctly classified subjects during the testing phase of each fold in the cross-validation strategy (see Section 2.2).

All performance measures are calculated based on the following classification outcomes:

- True positive (TP): The subject is truly positive and is classified as positive by the classifier.
- False positive (FP): The subject is truly negative but is classified as positive by the classifier.
- True negative (TN): The subject is truly negative and is classified as negative by the classifier.
- False negative (FN): The subject is truly positive but is classified as negative by the classifier.

All reported measures of performance are averages over five folds (5-fold cross validation). The sensitivity and specificity are computed as:

$$sensitivity = \frac{TP}{TP + FN} \quad (3.1)$$

and

$$specificity = \frac{TN}{TN + FP}. \quad (3.2)$$

The balanced accuracy is measured by determining the ratio of correctly classified subjects to the total considered subjects:

$$\text{balanced accuracy} = \frac{1}{2} \left(\frac{TP}{TP + FN} + \frac{TN}{TN + FP} \right), \quad (3.3)$$

which is equal to the arithmetic mean of the sensitivity and specificity. The balanced accuracy, in contrast to the ordinary accuracy, takes the number of subjects in each class into account. This makes classification of unbalanced datasets possible. The reference balanced accuracy is 50% (chance-level) for every experiment, irrelevant of the number of subjects in each class.

Sensitivity can be interpreted as the fraction of correctly classified patients when considering all truly positive participants. Specificity, on the other hand, is the fraction of correctly classified control subjects when considering all truly negative participants.

Chapter 3. Methods

Accuracy, sensitivity, and specificity are measured on a scale of 0 to 1. An accuracy of 1 represents a perfect agreement between our prediction and the subject labels determined by the psychiatrist. A score of 0 represents a misclassification of all subjects.

The test set for each classification experiment included five to six subjects, which were sampled differently in each of the five folds. I report the average performance over all folds in this thesis. However, one correct or incorrect classification can impact the classification outcome for one fold by a large margin. For example, the misclassification of one subject already decreases the accuracy by one-sixth or one-fifth (16.67% or 20%, respectively) for this fold. The results in Section 4 should, therefore, be viewed in this light.

The mean and median accuracy, sensitivity, and specificity, as well as the 95% confidence interval (CI) were used to evaluate the general performance of the models. These measures are calculated over the five folds. Moreover, two-sided t-tests were calculated on the saved results of the five-fold cross validation to compare model performances. The p values are reported, whereby a p value < 0.05 is considered statistically significant, which means that the models are significantly different from each other.

Chapter 4

Results

In this project, I created a pipeline for the classification of a dataset of 45 participants into subjects with psychosis and VH (PSVH^+), subjects with psychosis without VH (PSVH^-), and healthy controls (HC). The results of this work are presented with respect to the classification performance and interpretability of the feature weights in the following sections. All classification results are the mean over five folds (cross-validation strategy, Section 3.4). The red dashed line indicates the chance accuracy (50%, see Section 3.6) in all performance metric plots.

The coefficients of the SVM classifier are also visualized as predictive weight maps. Thereby, a high absolute weight indicates, that this feature was especially relevant for distinguishing between the groups. The sign of the weight demonstrates which class it contributes to in classification, while the magnitude of the weight indicates its importance. The weight matrices are presented for each group contrast (PSVH^+ vs. PSVH^- , PSVH^+ vs. HC, and PSVH^- vs. HC). All brain areas of interest were identified using the Brodmann atlas template in MRICron [101].

4.1 Classification of psychosis patients with and without visual hallucinations (PSVH^+ vs. PSVH^-)

In distinguishing between PSVH^+ and PSVH^- , three feature types yielded performances significantly above chance level: ReHo, and fALFF, VMHC. The mean classification performance of all feature types and feature vector sizes measured by accuracy, sensitivity, and specificity is shown in Figure 4.1. The median performance including the 95% CI over five folds is depicted in Figure 6.1 in the Appendix.

The highest performance was achieved using ReHo features and no feature selection (mean accuracy, sensitivity, and specificity of 66.67%, respectively, median accuracy of 66.67%, 95% CI [53.6%, 79.73%]). The corresponding weight matrices for all features, as well as the weights for ReHo with feature selection (10000 features) are presented in Figure 4.2. Several areas of the brain stand out as localized

Chapter 4. Results

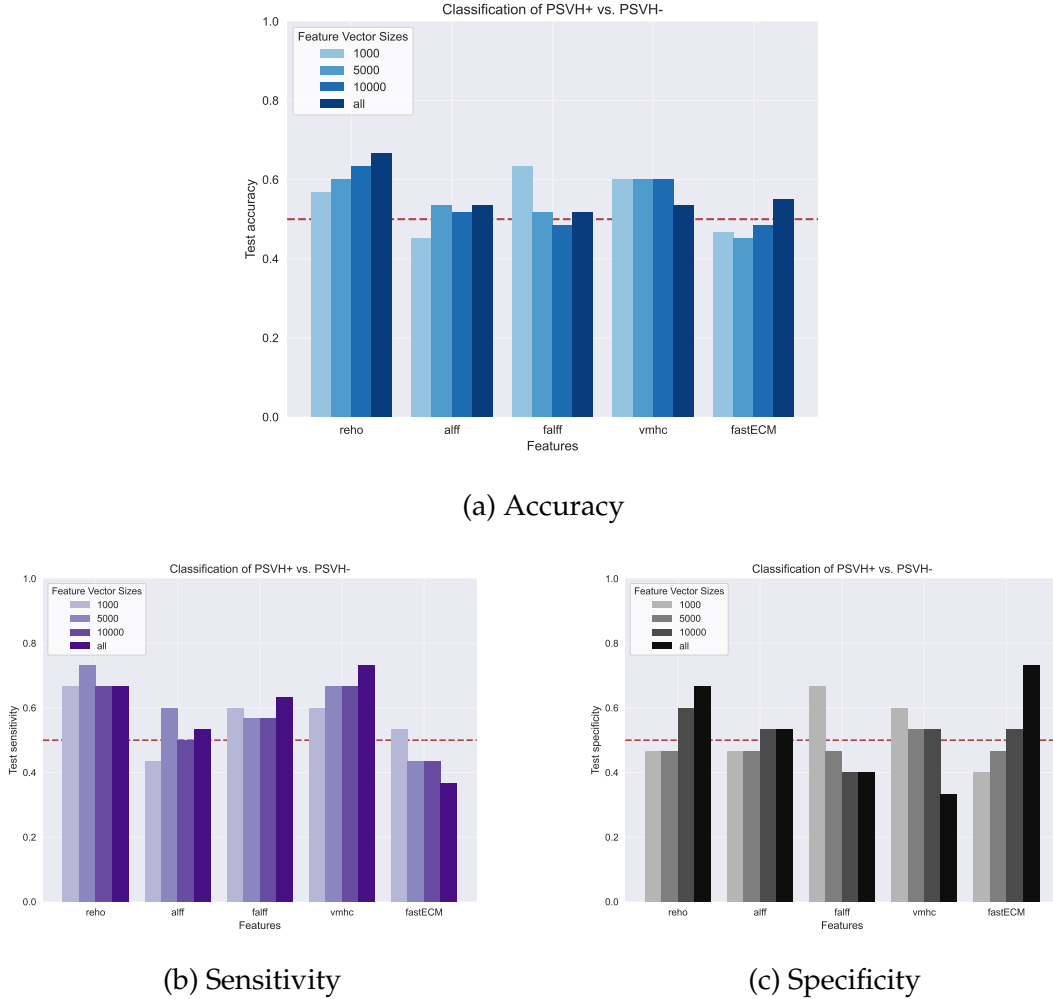


Figure 4.1: Mean performance measures for the classification of PSVH⁺ vs. PSVH⁻.

regions of high weight (red areas). The two red localized regions at slice $z = -9$ are located in the retrosubicular area (Brodmann area 48). Other areas with high predictive power are located in Brodmann area (BA) 18, the secondary visual cortex (V2) and in BA 19, the associative visual cortex (V3,V4,V5). Furthermore, the premotor and supplementary motor cortex (BA 6), as well as a part of the frontal cortex including the frontal eye fields (BA 8) were also found to be relevant to the SVM. Unilaterally on the left side of the brain, Broca's area (BA 45) also yielded a high predictive weight.

In addition, Figure 4.2 demonstrates that the feature selection process using Pearson correlation was able to extract the most relevant features from the ReHo data. Many of the regions in the lower image (ReHo, all) correspond well with the voxel regions in the upper image (ReHo with feature selection of the 10000 most salient features). However, the decrease in classification accuracy between ReHo with feature selection compared to ReHo without feature selection attests to the limitation of the current feature selection pipeline. Moreover, it should be noted that a

Chapter 4. Results

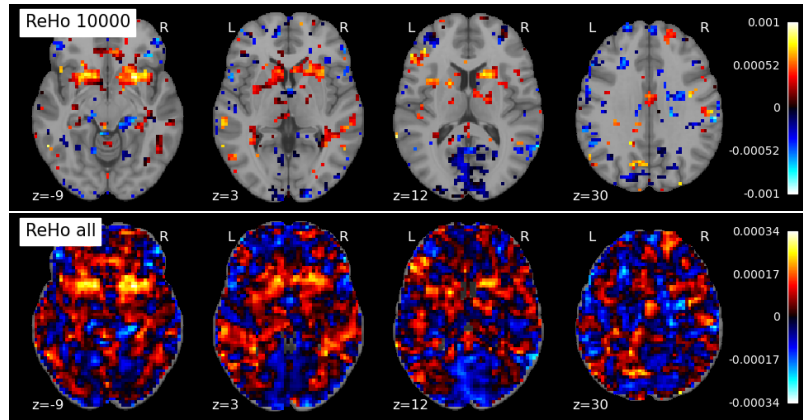


Figure 4.2: SVM weights for the classification of PSVH⁺ vs. PSVH⁻ using ReHo features with feature selection to 10000 features (top) and ReHo without feature selection (bottom).

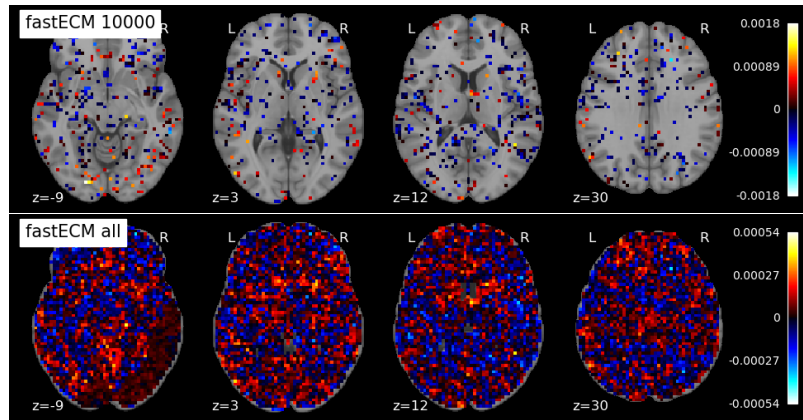


Figure 4.3: SVM weights for the classification of PSVH⁺ vs. PSVH⁻ using fastECM features with feature selection to 10000 features (top) and fastECM without feature selection (bottom).

post-hoc t-test revealed, that the difference between ReHo with feature selection and ReHo without feature selection is not statistically significant ($p > 0.05$).

The next best performing combinations of feature type and feature vector size were fALFF with 1000 features (mean accuracy of 63.33%, median accuracy of 66.67%, 95% CI [52.35%, 80.98%]), VMHC with 1000 features (mean accuracy of 60%, median accuracy of 66.67%, and 95% CI of [59.51%, 73.82%]) and VMHC with 5000 features (mean accuracy of 60%, median accuracy of 66.7%, and 95% CI of [51.77%, 81.56%]). Using fastECM without feature selection I achieved a mean accuracy of 55%, but the accuracy was not significantly different from chance (median accuracy of 50% and 95% CI [44.16%, 55.84%]). All other combinations had a performance that was not significantly different from the chance performance (see Figure 6.1). I found the sensitivity to be higher in general, except for the fastECM features. The highest mean sensitivity was achieved by ReHo with 5000 features

Chapter 4. Results

and VMHC without feature selection (73.3% and 73.3%, respectively). In contrast, the mean specificity was highest for fastECM without feature selection (73.3%). Because of the broad ranges of accuracies within the five folds, none of the models in this classification experiment had a statistically significant difference in performance from any of the other models (all $p > 0.05$).

The lowest classification performance was achieved by using fastECM features with 1000, 5000, and 10000 (mean accuracy of 46.67%, 45%, and 48.33%, respectively). Using fastECM without feature selection resulted in a higher accuracy (55%). However, this accuracy was not significantly different from chance (median accuracy of 50%, 95% CI [44.15%, 55.84%]) and also not significantly different from fastECM with feature selection ($p > 0.05$).

All corresponding SVM weight matrices are presented in Figure 4.3. In these predictive weight maps, one cannot clearly identify localized regions of high relevance. This is also reflected in the predictive weight map for fastECM with feature selection to 10000 voxels (Figure 4.3, top). Many of the voxels selected by Pearson correlation are visualized in blue and, therefore, are negatively correlated with the SVM's allocation of the positive label (PSVH⁺). The feature selection method likely decreased the performance of fastECM by selecting more features with negative contribution from the fastECM maps.

4.2 Classification of psychosis patients with visual hallucinations and healthy controls (PSVH⁺ vs. HC)

A considerably higher mean accuracy was achieved in distinguishing PSVH⁺ from HC, compared to the previously mentioned classification experiment (Section 4.1). All experiments yielded a mean accuracy at or above chance level and high sensitivity (Figure 4.4). Moreover, many of the median accuracies and sensitivities were significantly different from chance (Figure 6.3 in the Appendix).

VMHC features led to the highest mean accuracy (77.5%), whereby the feature vector size did not affect the classification outcome. This performance was also significantly different from chance (median accuracy of 83.33% and 95% CI [75.47%, 91.2%] for all feature vector sizes). This points to the fact that even a stark reduction of the feature vector size (902629 features without feature selection vs. 1000 features with feature selection) and computational cost, did not negatively affect the classification accuracy for VMHC. This is also supported by the post-hoc t-test result, which yielded $p \approx 1$ for all comparisons between the feature vector sizes for VMHC features (no statistically significant difference between the models). Employing VMHC features without feature selection differed in the mean sensitivity (80%) from VMHC with feature selection (86.7%). The highest mean specificity was found for VMHC without feature selection (75%). The corresponding SVM weight matrices for VMHC with and without feature selection are visualized in Figure 4.5.

Chapter 4. Results

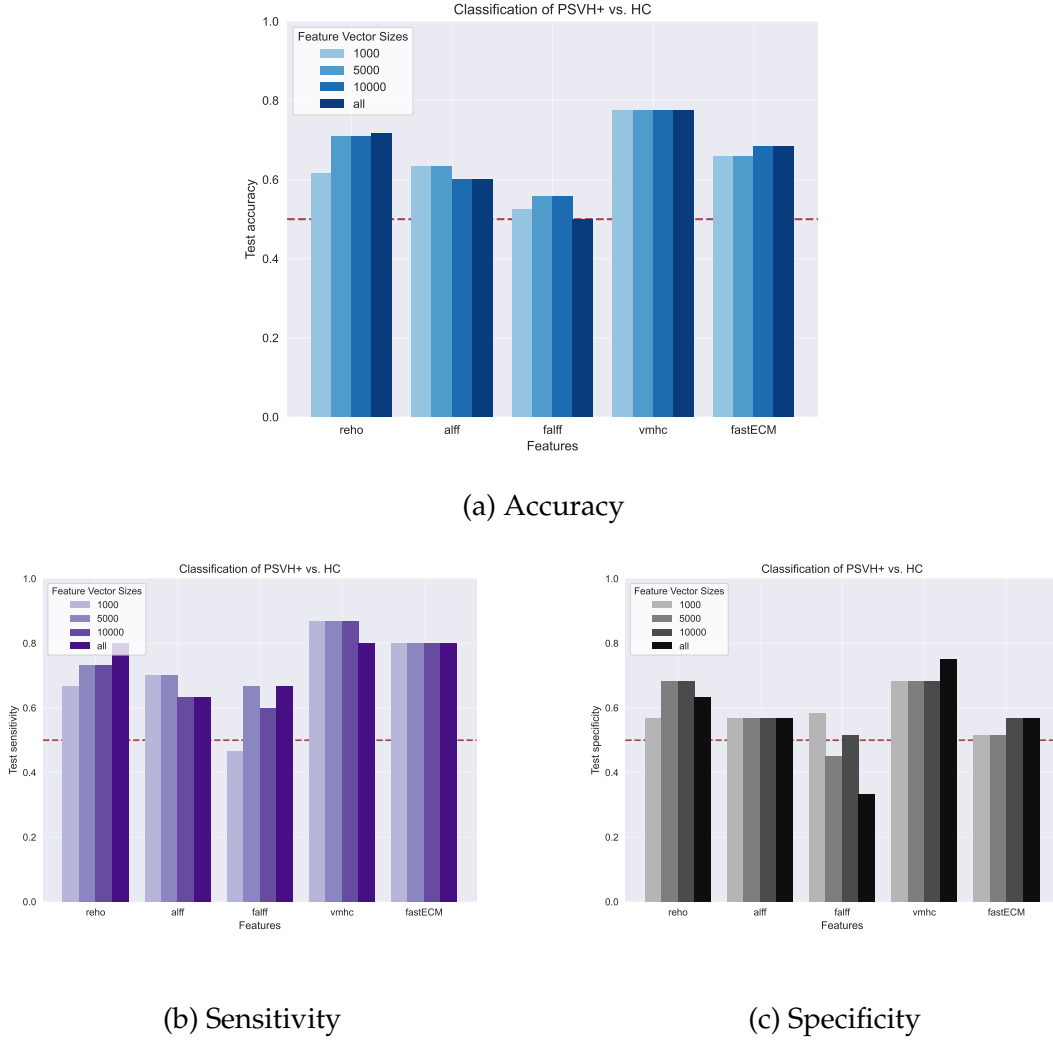


Figure 4.4: Mean performance measures for the classification of PSVH⁺ vs. HC.

A t-test yielded a statistically significant difference between the accuracy of the classifiers using VMHC and fastECM features with all feature vector sizes ($p = 0.0338$). The difference between ReHo and VMHC was not significant ($p > 0.05$), as was the difference between the accuracies of ReHo and fastECM ($p > 0.05$). The difference between the accuracies of fALFF, VMHC, and fastECM features was significant ($0.0002 < p < 0.02$), whereas these were not significantly different from ALFF and ReHo. The only significant comparison for fALFF and ReHo was found between ReHo without feature selection and fALFF without feature selection ($p = 0.008$). All accuracies were significantly above chance, except for ALFF with 10000 features and no feature selection (both median accuracy of 50%, 95% CI [38.31%, 61.69%]), fALFF features with 5000 and 10000 features (median accuracy of 50%, 95% CI [43.63%, 56.38%], respectively), and fALFF without feature selection (median accuracy of 50%, 95% CI [50%, 50%]).

Chapter 4. Results

The most prominent areas of high feature weight for the VMHC features are located in Broca's area (BA 45), the middle temporal gyrus (BA 21), the dorsal anterior cingulate area (BA 18) and parts of the cingulate cortex and parahippocampal gyrus (BA 23 and BA 27, respectively). Figure 4.5 also demonstrates, that the feature selection process was useful for identifying the most salient features for classification. The most prominent areas in Figure 4.5 (bottom) are also visible in Figure 4.5 (top).

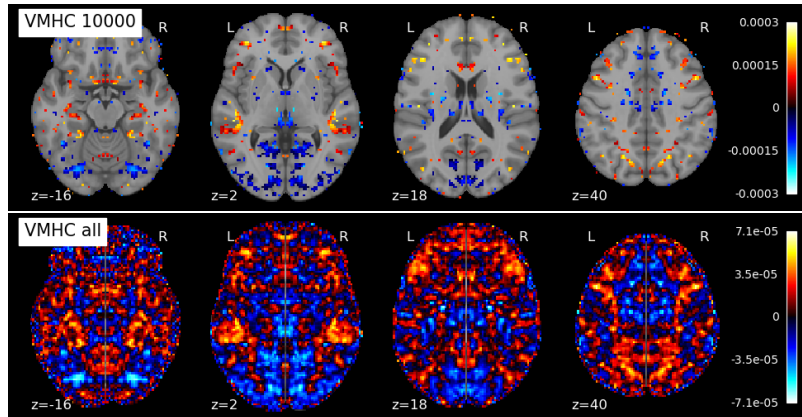


Figure 4.5: SVM weights for the classification of PSVH⁺ vs. HC using VMHC features with feature selection 10000 features (top) and VMHC without feature selection (bottom).

4.3 Classification of psychosis patients without visual hallucinations and healthy controls (PSVH⁻ vs. HC)

The classification of participants in the PSVH⁻ group and HC was performed as well to provide a reference for the other two experiments. The mean performance metrics for this classification experiment are summarized in Figure 4.6, whereas the median performance is summarized in Figure 6.5 in the Appendix. The best performing SVM classifier was trained on the most salient 1000 fastECM features after feature selection. This yielded a mean accuracy of 67.5%, mean sensitivity of 80%, and mean specificity of 55%. The median sensitivity for fastECM features with all feature vector sizes was 100% (95% CI [76.63%, 100%]). The predictive weight maps for the fastECM features with and without feature selection are presented in Figure 4.7. Four classifiers had a significantly different accuracy compared to the chance-level. These were fALFF with 5000 features (median accuracy of 66.67%, 95% CI [55.35%, 77.98%]), fastECM with 1000 features (median accuracy of 70.83%, 95% CI [54.76%, 86.90%]), and fastECM with 5000 and 10000 features (median accuracy of 66.67%, 95% CI [52.13%, 81.20%], respectively). None of the model accuracy comparisons in this classification experiment was statistically significant except for one: The difference between fALFF without feature selection and all other models that performed above-chance was significant ($p < 0.05$).

Chapter 4. Results

The fastECM feature weight matrices are hard to interpret by visual inspection. Therefore, I cannot identify localized regions of high feature weight. However, in comparison to the SVM weight maps for fastECM in the classification of PSVH⁺ vs. PSVH⁻ (Section 4.1 and Figure 4.3), the feature selection process yielded more positively correlated features with the positive label. The proportion of red features in the top three weight maps in Figure 4.7 is significantly higher, than the proportion of positive weights in Figure 4.3. An overview of all feature weight maps (pipeline without feature selection) can be seen in the Appendix.

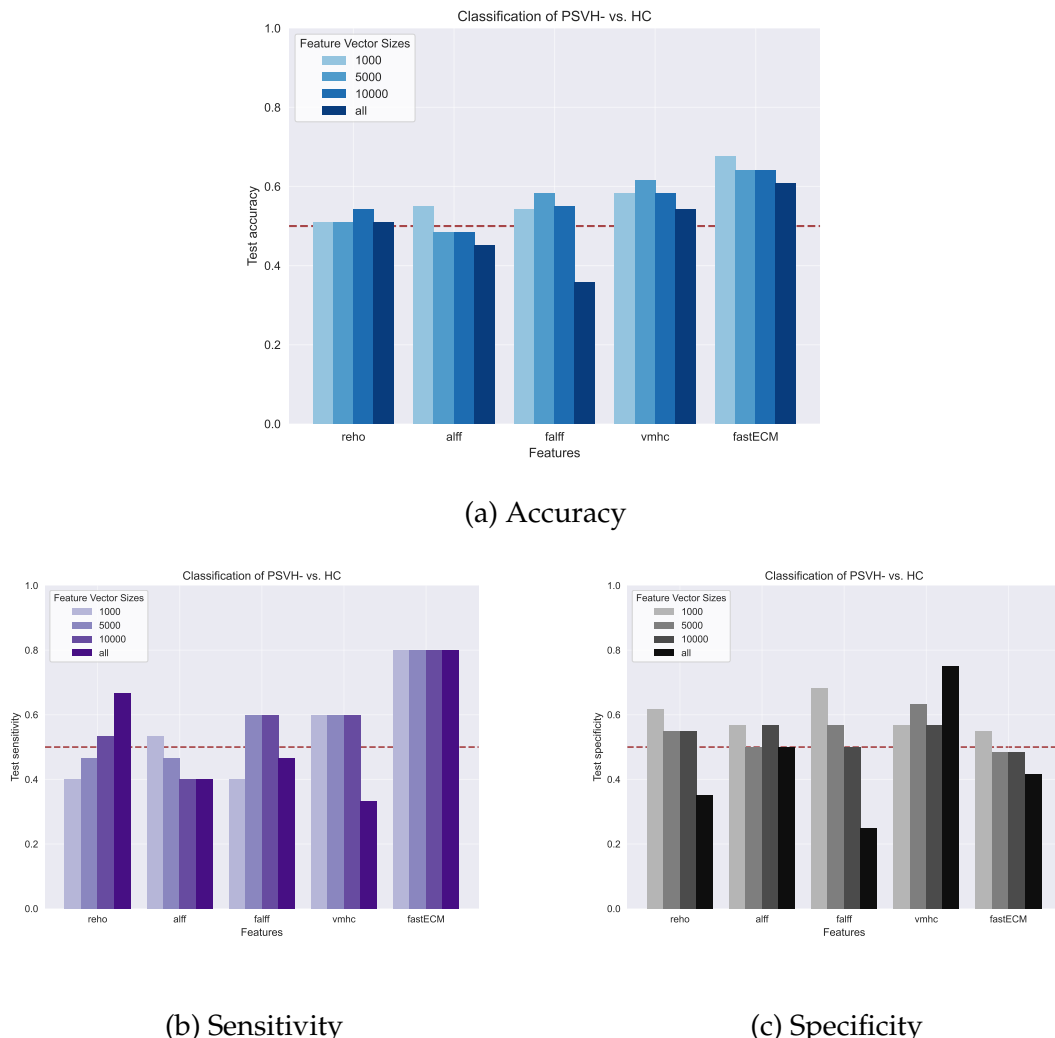


Figure 4.6: Mean performance measures for the classification of PSVH⁻ vs. HC.

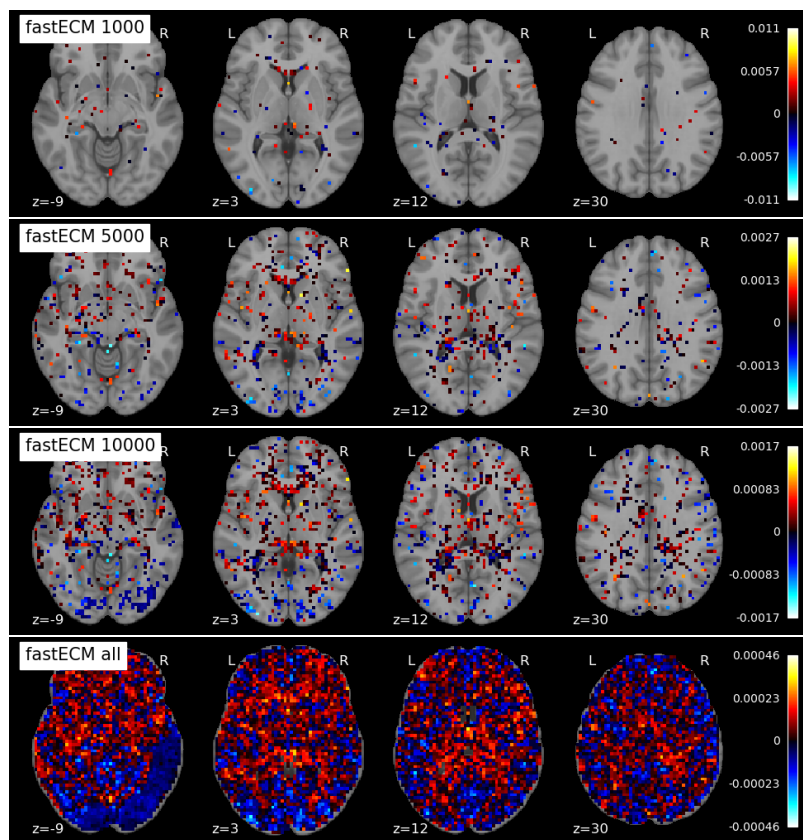


Figure 4.7: SVM weights for the classification of PSVH⁻ vs. HC using fastECM features with feature selection to 1000, 5000, and 10000 features, as well as fastECM features without feature selection (top to bottom).

Chapter 5

Discussion

In this thesis, an automated classification pipeline for the detection of lifetime VH was created and evaluated on a dataset comprised of 45 participants with and without psychosis. Several activity measures were compared with respect to their interpretability and classification performance. Moreover, the effect of using a feature selection procedure for dimensionality reduction was assessed. None of these features have been employed for the classification of VH in the literature. Therefore, this work might present a basis for future work on the classification of individuals experiencing VH using rs-fMRI and local activity measures.

Compared to previous studies examining VH [3, 44], that yielded below or at-chance accuracies in distinguishing between participants with and without VH, I was able to achieve a significantly above-chance accuracy in the classification of PSVH+ and PSVH- by using ReHo features (mean and median accuracy of 66.7%, 95% [53.6%, 79.73%]). This shows, that there are significant differences in neural activity between subjects in the PSVH+ and PSVH- groups, that can be exploited for classification using a linear SVM. However, a post-hoc t-test showed that none of the models in this experiment were significantly different from each other ($p > 0.05$). Therefore, these results should be viewed with caution and should be verified using a larger dataset. Nevertheless, the ReHo features yielded several localized regions of high predictive power that could be targets of future investigations on VH in psychosis, such as the retrosubicular area and the secondary and associative visual cortices (V2-V5).

Other areas with high weight point to opportunities for improvement in future studies. For example, the premotor and supplementary motor cortices, as well as Broca's area were found to have a high predictive weight in classification between PSVH⁺ and PSVH⁻ using ReHo features. This might be due to the amount and type of hallucinations experienced by the participants at scanning time. Seven subjects in the PSVH⁺ group experienced hallucinations while in the scanner, compared to only three subjects in the PSVH⁻ group. Participants in the PSVH⁺ group experienced frequent VH, AH and tactile hallucinations, while subjects in the PSVH⁻ group experienced only AH and tactile hallucinations. Given that more participants in the PSVH⁺ group experienced AH than in the PSVH⁻ group, the weight

Chapter 5. Discussion

of Broca's area, an area responsible for speech production which was frequently connected to the experience of AH [12, 46, 47], might be explained. Moreover, a difference in the amount of tactile hallucinations might have led to increased movement in the PSVH⁺ group, thereby activating the motor areas of the brain. In future work on the classification of VH, it might be useful to recruit participants with only one hallucination modality. This might yield more specific biomarkers for VH, that are not corrupted by neural activity stemming from AH and tactile hallucinations [44].

The distinction between PSVH⁺ and HC was also possible with at or above-chance level accuracy for all feature types and feature vector sizes. While VMHC features with feature selection yielded the highest mean accuracy (77.5%) and median accuracy (83.33%, 95% CI [75.47%, 91.20%]), it also yielded a high sensitivity (mean sensitivity of 86.7%, median sensitivity of 100%, 95% CI [[85.68%, 100%]). Furthermore, the feature weights were also visually interpretable. Localized regions of high weight were found, among others, in Broca's area, the middle temporal gyrus, and the dorsal anterior cingulate area. Given that VMHC measures mirrored homotopic connectivity, this feature especially identifies neural activity differences between the hemispheres. Since Broca's area is located only on the left side of the brain and is frequently involved in the experience of AH, the high weight of this area can be explained. Participants in the PSVH⁺ group had frequent AH, while the language areas were likely not activated in the HC group at scanning time. This yields a difference in the activation of Broca's area between PSVH⁺ and HC, which was exposed by VMHC. All other areas, that were found to have high predictive weight in the classification of PSVH⁺ and HC, were also connected to the neuropathology of hallucinations in the past. Abnormalities in the middle temporal gyrus [102], the (anterior) cingulate [103, 104, 105], and the parahippocampal gyrus [106] were identified in subjects with hallucinations before.

Given the amount of brain regions connected to AH that were found to have a high predictive weight in this experiment, these biomarkers likely represent AH, rather than VH. Therefore, the regions identified in Section 4.1 are more relevant for the detection of VH compared to the regions found in this experiment.

The high accuracy in distinguishing between PSVH⁺ and HC compared to the accuracies achieved in the other experiments (PSVH⁺ vs. PSVH⁻ and PSVH⁻ vs. HC) are possibly due to the disease severity of participants in the PSVH⁺ group. Psychosis and the experience of hallucinations are likely related to dysconnectivity in the brain [47, 107, 108]. This causes widespread differences in neural activity between individuals with psychosis and healthy controls, which can be exploited in the classification of these individuals using machine learning techniques. Furthermore, the participants in the PSVH⁺ group in my study have a higher psychosis disease severity compared to subjects in the PSVH⁻ group (see Section 3.1, PANSS and QPE scores). Thus, subjects in the PSVH⁺ group likely differ more from HC subjects, compared to individuals in the PSVH⁻ group. This, in turn, increases the classification accuracy on PSVH⁺ vs. HC.

Chapter 5. Discussion

Finally, I also classified PSVH⁻ and HC subjects. fastECM features were found to be superior to all other features in the classification of these two groups. While fastECM features and feature selection to 1000 salient voxels led to an accuracy of 67.5%, sensitivity of 80%, and specificity of 55%, the feature weights were not visually interpretable. The voxel-wise localizations provided by the SVM classifier did not point to one specific region of interest, that was most salient for distinguishing the groups. Rather, scattered voxels all over the brain were predictive of the subject label. In comparison, other features (such as VMHC, the next best classifier) did show a high predictive weight of language areas, such as Broca's area, for the classification of PSVH⁻ and HC. Therefore, even though fastECM yielded an above-chance accuracy (median accuracy of 70.83%, 95% CI [54.76%, 86.90%]), and an exceptionally high sensitivity (median sensitivity of 100%, 95% CI [76.62%, 100%]), the feature weights are not visually interpretable. Hence, the pipeline with fastECM features, feature selection, and an SVM classifier would be a less explainable option for application in the clinic.

Overall, it should be noted that a high classification weight does not directly indicate an underlying difference in neural activity in the corresponding brain region between the two groups. Rather, this region is particularly relevant to the SVM classifier. Regions of high predictive weight can, but must not correlate with an underlying brain mechanism [109]. More traditional neuroscientific studies targeting the aforementioned brain regions are, therefore, necessary to uncover neuronal activity patterns ultimately responsible for the experience of VH.

The dataset used for classification in this study also was likely not optimally suited for the task of classifying VH. All participants in the PS groups experienced some modality of hallucinations (f.e. AH or tactile hallucinations). This leads to a mixed group of subjects, whereby VH only occur in combination with other hallucination modalities. To disentangle the neural correlates of VH from AH and tactile hallucinations, it would be preferable to examine a group of individuals with only VH. However, individuals with psychosis and only VH are rare. This makes it difficult to find an optimal dataset for this feat.

The above-mentioned point is also underpinned by the large variance in accuracy between folds found in the classification of this dataset. In many experiments, the accuracy between folds varied approximately between 50% and 83%. When the algorithm is trained on the data of certain individuals, it performs better in the testing phase. This leads me to think that more homogeneous samples of the three subject groups (f.e. subjects with psychosis and only VH, subjects with psychosis without any hallucinations, and HC) might lead to better results in classification and more specific biomarkers for VH.

Computationally, it stands to reason that feature selection often does not significantly improve the overall classification results and might affect some feature types in a negative way. For example, feature selection by Pearson correlation on the VMHC features did not lead to a large decrease in accuracy in classification

Chapter 5. Discussion

of PSVH⁺ and HC (Figure 4.4a). On the other hand, the fastECM, ALFF, and ReHo features suffered from decreases in accuracy when feature selection was applied in distinguishing PSVH⁺ from PSVH⁻ (Figure 4.1a). While ReHo without feature selection led to an above-chance level accuracy, the median accuracy of ReHo with 1000, 5000, and 10000 selected features lies at 50%. Given that Pearson correlation can only identify linear correlations between the voxel intensities and the corresponding class labels, it stands to reason that a non-linear or machine learning-based feature selection method might be more suitable here.

Chapter 6

Conclusion and future work

The findings obtained in this research project suggest that the classification of lifetime VH in the individuals with psychosis that I assessed is achievable. Five different feature extraction methods, a feature selection procedure, as well as a linear SVM classifier, were employed to classify rs-fMRI images of individuals with psychosis, as well as healthy controls. ReHo features without feature selection proved to be best in distinguishing PSVH⁺ from PSVH⁻, while VMHC features yielded the best result in the classification of PSVH⁺ and HC. Finally, fastECM features with feature selection led to the best classification accuracy in discriminating between PSVH⁻ and HC.

Although above-chance level accuracies were obtained for each classification experiment, several limitations of this study should be noted. The first major limitation is the sample size. In total, the data of 45 participants were analyzed, whereby each group contains 14 to 16 participants. Therefore, in the binary classification of the groups, only 29 to 31 participants were considered per experiment. While this is a considerable size given the prevalence of VH in the general population, it is likely not suitable for making predictions on a larger scale. Hence, this study should be repeated on a larger multi-site dataset including more participants with VH. Furthermore, the dataset I used in my study contains data from individuals with both VH and other hallucination modalities. To obtain biomarkers of VH, it might be useful and necessary in the future to study individuals experiencing only VH.

The post-hoc t-tests on the accuracy of the models also showed mixed results. In the PSVH⁺ vs. PSVH⁻ there was no statistically significant difference between the models. A similar pattern was found for the PSVH⁻ vs. HC experiment. The only experiment, where many statistically significant differences between the models was found is PSVH⁺ vs. HC. Therefore, the presented results should be viewed with caution. Given the small sample size and the large range of classification performances over folds, the confidence intervals are rather large. This could likely be improved on by repeating this study on a larger sample.

Chapter 6. Conclusion and future work

From a computational side, I found that feature selection by Pearson correlation applied to the current dataset often did not improve or even worsen the results in classification. This might be due to the feature selection procedure employed. Especially fastECM and ReHo features in the classification of PSVH⁺ vs. PSVH⁻ suffered from applying feature selection. The feature weight maps for this feature type also underpin this fact. The feature maps for fastECM with feature selection show sparsely distributed single voxels that do not show a consistent pattern. This suggests that the most relevant voxels were discarded of when applying Pearson correlation to fastECM features. For ReHo, the feature selection process yielded condensed regions of high importance. Nevertheless, the accuracy decreased when using feature selection. This leads me to think, that the feature selection procedure should be tailored to each feature type individually to exploit the characteristics of the different activity maps. On the other hand, several feature types did not suffer from or even improved in accuracy when feature selection was applied, such as VMHC. Given the improvement in computational efficiency when feature selection is used, this is a good indicator of the usefulness of performing feature selection in this project. In future studies, non-linear or machine learning-based feature selection procedures could be tested to evaluate their usefulness in the classification of lifetime VH.

The classification algorithm could likely also be improved. While SVMs yielded good performances in schizophrenia and hallucination detection in the past, they are not the only option for the classification of rs-fMRI images. Other machine learning methods, such as random forests or extreme learning machines, as well as deep learning methods were useful in classification of schizophrenia using fMRI as well as structural MRI images in the past [40, 41, 49, 110, 111, 112, 113, 114, 115, 116]. It stands to reason that these techniques could potentially yield good performances in the classification of lifetime VH as well and, therefore, should be investigated further. Some of these methods can even exploit the information encoded in rs-fMRI images directly, without the need for local feature extraction. This might yield different patterns of activity that are correlated with the appearance of VH. However, the sample size is a major limitation in training of deep learning classifiers, since these complex models require large amounts of training data. One possible method to overcome this limitation is transfer learning [38]. Thereby, a machine or deep learning model is initially trained on a different task (f.e. schizophrenia detection) and subsequently applied to the classification of other pathologies (f.e. visual hallucinations). Several papers investigated the classification of medical imaging data using transfer learning [117, 118, 119, 120]. Given the good availability of larger datasets of individuals with schizophrenia and healthy controls, such as the COBRE dataset [42], transfer learning for the detection of lifetime VH might be feasible in the future.

Even though high accuracies and sensitivities were achieved in this project, the trained classifiers are not yet suitable for application in the clinic. Given the negative impact a misclassification can have on the affected individual, the sensitivity

Chapter 6. Conclusion and future work

and specificity should be significantly improved before a clinical use of the created algorithm can be considered. Moreover, there is a large gap in explainability between the feature types. While ReHo and VMHC offered more explainable SVM weight maps with localized and identifiable regions of high feature weight, the other feature types yielded more scattered feature maps. Clinical professionals would likely not be able to draw conclusions about the functioning of the SVM classifier from these scattered maps. Furthermore, training of the SVM on a much larger dataset from multiple scanners should be conducted to be able to use it for prediction of lifetime VH in a clinical setting. Nevertheless, my results provide a good baseline for future research on the classification of lifetime VH in individuals with psychosis.

Bibliography

- [1] Flavie Waters, Daniel Collerton, Dominic H. ffytche, Renaud Jardri, Delphine Pins, Robert Dudley, Jan Dirk Blom, Urs Peter Mosimann, Frank Eperjesi, Stephen Ford, and Frank Larøi. Visual Hallucinations in the Psychosis Spectrum and Comparative Information From Neurodegenerative Disorders and Eye Disease. *Schizophrenia Bulletin*, 40(Suppl 4):S233–S245, July 2014.
- [2] Ryan C. Teeple, Jason P. Caplan, and Theodore A. Stern. Visual Hallucinations: Differential Diagnosis and Treatment. *Primary Care Companion to The Journal of Clinical Psychiatry*, 11(1):26–32, 2009.
- [3] Maya JL Schutte, Marc M. Bohlken, Guusje Collin, Lucija Abramovic, Marco PM Boks, Wiepke Cahn, Meenakshi Dauwan, Edwin van Dellen, Neeltje EM van Haren, and Kenneth Hugdahl. Functional connectome differences in individuals with hallucinations across the psychosis continuum. *Scientific reports*, 11(1):1–13, 2021.
- [4] Marouska Manouk van Ommen, Azzurra Invernizzi, Remco Jan Renken, Richard Bruggeman, Frans Cornelissen, and Teus van Laar. Impaired functional connectivity in patients with psychosis and visual hallucinations. *medRxiv*, 2022.
- [5] Peggy Series, David Reichert, and Amos J. Storkey. Hallucinations in Charles Bonnet syndrome induced by homeostasis: A deep Boltzmann machine model. *Advances in Neural Information Processing Systems*, 23, 2010.
- [6] David P. Reichert, Peggy Series, and Amos J. Storkey. Homeostasis causes hallucinations in a hierarchical generative model of the visual cortex: The Charles Bonnet Syndrome. *BMC Neuroscience*, 12(1):P319, July 2011.
- [7] Linda Pang. Hallucinations Experienced by Visually Impaired: Charles Bonnet Syndrome. *Optometry and Vision Science*, 93(12):1466–1478, December 2016.
- [8] Andreas Meyer-Lindenberg. Neural connectivity as an intermediate phenotype: Brain networks under genetic control. *Human brain mapping*, 30(7):1938–1946, 2009.

Chapter 6. Bibliography

- [9] M. M. Bohlken, K. Hugdahl, and I. E. C. Sommer. Auditory verbal hallucinations: Neuroimaging and treatment. *Psychological Medicine*, 47(2):199–208, January 2017.
- [10] Joshua B. Tan, Eli J. Müller, Isabella F. Orlando, Natasha L. Taylor, Daniel S. Margulies, Jennifer Szeto, Simon J. G. Lewis, James M. Shine, and Claire O’Callaghan. Abnormal higher-order network interactions in Parkinson’s disease visual hallucinations, April 2023.
- [11] Rowena Carter. On visual hallucinations and cortical networks: A trans-diagnostic review. *Journal of neurology*, 262(7):1780–1790, 2015.
- [12] Ann K. Shinn, Justin T. Baker, Bruce M. Cohen, and Dost Öngür. Functional connectivity of left Heschl’s gyrus in vulnerability to auditory hallucinations in schizophrenia. *Schizophrenia Research*, 143(2):260–268, February 2013.
- [13] Ben Alderson-Day, Kelly Diederen, Charles Fernyhough, Judith M. Ford, Guillermo Horga, Daniel S. Margulies, Simon McCarthy-Jones, Georg Northoff, James M. Shine, Jessica Turner, Vincent van de Ven, Remko van Luttermeld, Flavie Waters, and Renaud Jardri. Auditory Hallucinations and the Brain’s Resting-State Networks: Findings and Methodological Observations. *Schizophrenia Bulletin*, 42(5):1110–1123, September 2016.
- [14] James M. Shine, Claire O’Callaghan, Glenda M. Halliday, and Simon JG Lewis. Tricks of the mind: Visual hallucinations as disorders of attention. *Progress in neurobiology*, 116:58–65, 2014.
- [15] James M. Shine, Alana J. Muller, Claire O’Callaghan, Michael Hornberger, Glenda M. Halliday, and Simon JG Lewis. Abnormal connectivity between the default mode and the visual system underlies the manifestation of visual hallucinations in Parkinson’s disease: A task-based fMRI study. *npj Parkinson’s Disease*, 1(1):1–8, April 2015.
- [16] Na Young Kim, Joey Hsu, Daniel Talmasov, Juho Joutsa, Louis Soussand, Ona Wu, Natalia S. Rost, Estrella Morenas-Rodríguez, Joan Martí-Fàbregas, Alvaro Pascual-Leone, Philip R. Corlett, and Michael D. Fox. Lesions causing hallucinations localize to one common brain network. *Molecular Psychiatry*, 26(4):1299–1309, April 2021.
- [17] Danilo Bzdok, Naomi Altman, and Martin Krzywinski. Statistics versus machine learning. *Nature Methods*, 15(4):233–234, April 2018.
- [18] Walid Yassin, Hironori Nakatani, Yinghan Zhu, Masaki Kojima, Keiho Owada, Hitoshi Kuwabara, Wataru Gono, Yuta Aoki, Hidemasa Takao, Tatsumonbu Natsubori, Norichika Iwashiro, Kiyoto Kasai, Yukiko Kano, Osamu Abe, Hidenori Yamasue, and Shinsuke Koike. Machine-learning classification using neuroimaging data in schizophrenia, autism, ultra-high risk and first-episode psychosis. *Translational Psychiatry*, 10(1):278, August 2020.

Chapter 6. Bibliography

- [19] Lorenzo Del Fabro, Elena Bondi, Francesca Serio, Eleonora Maggioni, Armando D'Agostino, and Paolo Brambilla. Machine learning methods to predict outcomes of pharmacological treatment in psychosis. *Translational Psychiatry*, 13(1):1–15, March 2023.
- [20] Ashkan Nejad, Saeed Masoudnia, and Mohammad-Reza Nazem-Zadeh. A Fast and Memory-Efficient Brain MRI Segmentation Framework for Clinical Applications. In *2022 44th Annual International Conference of the IEEE Engineering in Medicine & Biology Society (EMBC)*, pages 2140–2143. IEEE, 2022.
- [21] Duaa AlSaeed and Samar Fouad Omar. Brain MRI analysis for Alzheimer's disease diagnosis using CNN-based feature extraction and machine learning. *Sensors*, 22(8):2911, 2022.
- [22] Karl-Heinz Nenning and Georg Langs. Machine learning in neuroimaging: From research to clinical practice. *Die Radiologie*, 62(1):1–10, December 2022.
- [23] Nalini M. Singh, Jordan B. Harrod, Sandya Subramanian, Mitchell Robinson, Ken Chang, Suheyla Cetin-Karayumak, Adrian Vasile Dalca, Simon Eickhoff, Michael Fox, Loraine Franke, Polina Golland, Daniel Haehn, Juan Eugenio Iglesias, Lauren J. O'Donnell, Yangming Ou, Yogesh Rathi, Shan H. Siddiqi, Haoqi Sun, M. Brandon Westover, Susan Whitfield-Gabrieli, and Randy L. Gollub. How Machine Learning is Powering Neuroimaging to Improve Brain Health. *Neuroinformatics*, 20(4):943–964, October 2022.
- [24] Bas HM van der Velden, Hugo J. Kuijf, Kenneth GA Gilhuijs, and Max A. Viergever. Explainable artificial intelligence (XAI) in deep learning-based medical image analysis. *Medical Image Analysis*, page 102470, 2022.
- [25] Jerry Tang, Amanda LeBel, Shailee Jain, and Alexander G. Huth. Semantic reconstruction of continuous language from non-invasive brain recordings. *Nature Neuroscience*, 26(5):858–866, May 2023.
- [26] R. J. Howard, M. J. Brammer, A. David, P. Woodruff, and S. Williams. The anatomy of conscious vision: An fMRI study of visual hallucinations. *Nature neuroscience*, 1(8):738–742, 1998.
- [27] Joel Weijia Lai, Candice Ke En Ang, U. Rajendra Acharya, and Kang Hao Cheong. Schizophrenia: A survey of artificial intelligence techniques applied to detection and classification. *International journal of environmental research and public health*, 18(11):6099, 2021.
- [28] Darya Chyzyk, Manuel Graña, Döst Öngür, and Ann K. Shinn. Discrimination of schizophrenia auditory hallucinators by machine learning of resting-state functional MRI. *International Journal of Neural Systems*, 25(03):1550007, 2015.

Chapter 6. Bibliography

- [29] Lanxin Ji, Shashwath A. Meda, Carol A. Tamminga, Brett A. Clementz, Matcheri S. Keshavan, John A. Sweeney, Elliot S. Gershon, and Godfrey D. Pearlson. Characterizing functional regional homogeneity (ReHo) as a B-SNIP psychosis biomarker using traditional and machine learning approaches. *Schizophrenia Research*, 215:430–438, January 2020.
- [30] Haihong Liu, Zhenling Liu, Meng Liang, Yihui Hao, Lihua Tan, Fan Kuang, Yanhong Yi, Lin Xu, and Tianzi Jiang. Decreased regional homogeneity in schizophrenia: A resting state functional magnetic resonance imaging study. *Neuroreport*, 17(1):19–22, 2006.
- [31] Shuai Wang, Yan Zhang, Luxian Lv, Renrong Wu, Xiaoduo Fan, Jingping Zhao, and Wenbin Guo. Abnormal regional homogeneity as a potential imaging biomarker for adolescent-onset schizophrenia: A resting-state fMRI study and support vector machine analysis. *Schizophrenia Research*, 192:179–184, February 2018.
- [32] Matthew J. Hoptman, Xi-Nian Zuo, Debra D’Angelo, Cristina J. Mauro, Pamela D. Butler, Michael P. Milham, and Daniel C. Javitt. Decreased interhemispheric coordination in schizophrenia: A resting state fMRI study. *Schizophrenia Research*, 141(1):1–7, October 2012.
- [33] Jessica Turner, Eswar Damaraju, Theo Van Erp, Daniel Mathalon, Judith Ford, James Voyvodic, Bryon Mueller, Aysenil Belger, Juan Bustillo, Sarah McEwen, Steven Potkin, Functional Imaging BIRN, and Vince Calhoun. A multi-site resting state fMRI study on the amplitude of low frequency fluctuations in schizophrenia. *Frontiers in Neuroscience*, 7, 2013.
- [34] Wenjing Zhu, Shoufeng Shen, and Zhijun Zhang. Improved Multiclassification of Schizophrenia Based on Xgboost and Information Fusion for Small Datasets. *Computational and Mathematical Methods in Medicine*, 2022:1581958, July 2022.
- [35] Renato de Filippis, Elvira Anna Carbone, Raffaele Gaetano, Antonella Bruni, Valentina Pugliese, Cristina Segura-Garcia, and Pasquale De Fazio. Machine learning techniques in a structural and functional MRI diagnostic approach in schizophrenia: A systematic review. *Neuropsychiatric Disease and Treatment*, 15:1605–1627, June 2019.
- [36] Geetha Soujanya Chilla, Ling Yun Yeow, Qian Hui Chew, Kang Sim, and K. N. Bhanu Prakash. Machine learning classification of schizophrenia patients and healthy controls using diverse neuroanatomical markers and Ensemble methods. *Scientific Reports*, 12(1):2755, February 2022.
- [37] Sunil Vasu Kalmady, Russell Greiner, Rimjhim Agrawal, Venkataram Shivakumar, Janardhanan C. Narayanaswamy, Matthew R. G. Brown, Andrew J. Greenshaw, Serdar M. Dursun, and Ganesan Venkatasubramanian. Towards

Chapter 6. Bibliography

- artificial intelligence in mental health by improving schizophrenia prediction with multiple brain parcellation ensemble-learning. *npj Schizophrenia*, 5(1):1–11, January 2019.
- [38] Meenakshi Khosla, Keith Jamison, Gia H. Ngo, Amy Kuceyeski, and Mert R. Sabuncu. Machine learning in resting-state fMRI analysis. *Magnetic resonance imaging*, 64:101–121, 2019.
 - [39] Elisa Veronese, Umberto Castellani, Denis Peruzzo, Marcella Bellani, and Paolo Brambilla. Machine learning approaches: From theory to application in schizophrenia. *Computational and mathematical methods in medicine*, 2013, 2013.
 - [40] Alexandre Savio and Manuel Graña. Local activity features for computer aided diagnosis of schizophrenia on resting-state fMRI. *Neurocomputing*, 164:154–161, September 2015.
 - [41] Darya Chyzyk, Alexandre Savio, and Manuel Graña. Computer aided diagnosis of schizophrenia on resting state fMRI data by ensembles of ELM. *Neural Networks*, 68:23–33, August 2015.
 - [42] The Mind Research Network (MRN). COBRE. <http://cobre.mrn.org/>, 2020.
 - [43] Arthur W. Toga, Kristi A. Clark, Paul M. Thompson, David W. Shattuck, and John Darrell Van Horn. Mapping the Human Connectome. *Neurosurgery*, 71(1):1–5, July 2012.
 - [44] Amicie de Pierrefeu, Thomas Fovet, Fouad Hadj-Selem, Tommy Löfstedt, Philippe Ciuci, Stephanie Lefebvre, Pierre Thomas, Renaud Lopes, Renaud Jardri, and Edouard Duchesnay. Prediction of activation patterns preceding hallucinations in patients with schizophrenia using machine learning with structured sparsity. *Human brain mapping*, 39(4):1777–1788, 2018.
 - [45] Jan Dirk Blom. Hallucinations and Other Sensory Deceptions in Psychiatric Disorders. In Renaud Jardri, Arnaud Cachia, Pierre Thomas, and Delphine Pins, editors, *The Neuroscience of Hallucinations*, pages 43–57. Springer, New York, NY, 2013.
 - [46] Thomas Fovet, Pierre Yger, Renaud Lopes, Amicie de Pierrefeu, Edouard Duchesnay, Josselin Houenou, Pierre Thomas, Sébastien Szaffarczyk, Philippe Domenech, and Renaud Jardri. Decoding Activity in Broca’s Area Predicts the Occurrence of Auditory Hallucinations Across Subjects. *Biological Psychiatry*, 91(2):194–201, January 2022.
 - [47] Branislava Ćurčić-Blake, Judith M. Ford, Daniela Hubl, Natasza D. Orlov, Iris E. Sommer, Flavie Waters, Paul Allen, Renaud Jardri, Peter W. Woodruff, Olivier David, Christoph Mulert, Todd S. Woodward, and André Aleman. Interaction of language, auditory and memory brain networks in auditory verbal hallucinations. *Progress in Neurobiology*, 148:1–20, January 2017.

Chapter 6. Bibliography

- [48] Manuel Graña, Leire Ozaeta, and Darya Chyzyk. Dynamic Causal Modeling and machine learning for effective connectivity in Auditory Hallucination. *Neurocomputing*, 326:61–68, 2019.
- [49] Muhammad Naveed Iqbal Qureshi, Jooyoung Oh, and Boreom Lee. 3D-CNN based discrimination of schizophrenia using resting-state fMRI. *Artificial Intelligence in Medicine*, 98:10–17, July 2019.
- [50] Madiha J. Jafri and Vince D. Calhoun. Functional Classification of Schizophrenia Using Feed Forward Neural Networks. In *2006 International Conference of the IEEE Engineering in Medicine and Biology Society*, volume Supplement, pages 6631–6634, August 2006.
- [51] Manuel Graña, Leire Ozaeta, and Darya Chyzyk. Resting State Effective Connectivity Allows Auditory Hallucination Discrimination. *International Journal of Neural Systems*, 27(05):1750019, August 2017.
- [52] Yufeng Zang, Tianzi Jiang, Yingli Lu, Yong He, and Lixia Tian. Regional homogeneity approach to fMRI data analysis. *Neuroimage*, 22(1):394–400, 2004.
- [53] Benito de Celis Alonso, Silvia Hidalgo Tobón, Pilar Dies Suarez, Julio García Flores, Benito de Celis Carrillo, and Eduardo Barragán Pérez. A multi-methodological MR resting state network analysis to assess the changes in brain physiology of children with ADHD. *PloS one*, 9(6):e99119, 2014.
- [54] Li An, Qing-Jiu Cao, Man-Qiu Sui, Li Sun, Qi-Hong Zou, Yu-Feng Zang, and Yu-Feng Wang. Local synchronization and amplitude of the fluctuation of spontaneous brain activity in attention-deficit/hyperactivity disorder: A resting-state fMRI study. *Neuroscience bulletin*, 29:603–613, 2013.
- [55] Xiaoxin Zhao, Jingjing Yao, Yiding Lv, Xinyue Zhang, Chongyang Han, Lijun Chen, Fangfang Ren, Zhuma Jin, Yuan Li, and Yuxiu Sui. Abnormalities of regional homogeneity and its correlation with clinical symptoms in Naïve patients with first-episode schizophrenia. *Brain imaging and behavior*, 13:503–513, 2019.
- [56] Yongjie Xu, Chuanjun Zhuo, Wen Qin, Jiajia Zhu, and Chunshui Yu. Altered spontaneous brain activity in schizophrenia: A meta-analysis and a large-sample study. *BioMed research international*, 2015, 2015.
- [57] Rongjun Yu, Ming H. Hsieh, Hsiao-Lan Sharon Wang, Chih-Min Liu, Chen-Chung Liu, Tzung-Jeng Hwang, Yi-Ling Chien, Hai-Gwo Hwu, and Wen-Yih Isaac Tseng. Frequency dependent alterations in regional homogeneity of baseline brain activity in schizophrenia. *PloS one*, 8(3):e57516, 2013.
- [58] M. Kendall and J. D. Gibbons. Rank Correlation Methods, 1990.

Chapter 6. Bibliography

- [59] Child Mind Institute. C-PAC (Python package). <https://fcp-indi.github.io/docs/latest/user/>, 2018.
- [60] Norman Geschwind. Language and the brain. *Scientific American*, 226(4):76–83, 1972.
- [61] Xi-Nian Zuo, Clare Kelly, Adriana Di Martino, Maarten Mennes, Daniel S. Margulies, Saroja Bangaru, Rebecca Grzadzinski, Alan C. Evans, Yu-Feng Zang, and F. Xavier Castellanos. Growing together and growing apart: Regional and sex differences in the lifespan developmental trajectories of functional homotopy. *Journal of Neuroscience*, 30(45):15034–15043, 2010.
- [62] Xiao Chang, Yi-Bin Xi, Long-Biao Cui, Hua-Ning Wang, Jin-Bo Sun, Yuan-Qiang Zhu, Peng Huang, Guusje Collin, Kang Liu, and Min Xi. Distinct interhemispheric dysconnectivity in schizophrenia patients with and without auditory verbal hallucinations. *Scientific Reports*, 5(1):1–12, 2015.
- [63] Raymond Salvador, John Suckling, Martin R. Coleman, John D. Pickard, David Menon, and E. D. Bullmore. Neurophysiological architecture of functional magnetic resonance images of human brain. *Cerebral cortex*, 15(9):1332–1342, 2005.
- [64] David E. Stark, Daniel S. Margulies, Zarrar E. Shehzad, Philip Reiss, AM Clare Kelly, Lucina Q. Uddin, Dylan G. Gee, Amy K. Roy, Marie T. Banich, and F. Xavier Castellanos. Regional variation in interhemispheric coordination of intrinsic hemodynamic fluctuations. *Journal of Neuroscience*, 28(51):13754–13764, 2008.
- [65] Zang Yu-Feng, He Yong, Zhu Chao-Zhe, Cao Qing-Jiu, Sui Man-Qiu, Liang Meng, Tian Li-Xia, Jiang Tian-Zi, and Wang Yu-Feng. Altered baseline brain activity in children with ADHD revealed by resting-state functional MRI. *Brain and Development*, 29(2):83–91, 2007.
- [66] Paul A. Taylor, Suril Gohel, Xin Di, Martin Walter, and Bharat B. Biswal. Functional Covariance Networks: Obtaining Resting-State Networks from Intersubject Variability. *Brain Connectivity*, 2(4):203–217, August 2012.
- [67] Qi-Hong Zou, Chao-Zhe Zhu, Yihong Yang, Xi-Nian Zuo, Xiang-Yu Long, Qing-Jiu Cao, Yu-Feng Wang, and Yu-Feng Zang. An improved approach to detection of amplitude of low-frequency fluctuation (ALFF) for resting-state fMRI: Fractional ALFF. *Journal of neuroscience methods*, 172(1):137–141, 2008.
- [68] Alle Meije Wink. Eigenvector Centrality Dynamics From Resting-State fMRI: Gender and Age Differences in Healthy Subjects. *Frontiers in Neuroscience*, 13, 2019.
- [69] Gabriele Lohmann, Daniel S. Margulies, Annette Horstmann, Burkhard Pleger, Joeran Lepsien, Dirk Goldhahn, Haiko Schloegl, Michael Stumvoll, Arno Villringer, and Robert Turner. Eigenvector Centrality Mapping for

Chapter 6. Bibliography

- Analyzing Connectivity Patterns in fMRI Data of the Human Brain. *PLOS ONE*, 5(4):e10232, April 2010.
- [70] Alle Meije Wink, Jan C. de Munck, Ysbrand D. van der Werf, Odile A. van den Heuvel, and Frederik Barkhof. Fast Eigenvector Centrality Mapping of Voxel-Wise Connectivity in Functional Magnetic Resonance Imaging: Implementation, Validation, and Interpretation. *Brain Connectivity*, 2(5):265–274, October 2012.
 - [71] Maja AA Binnewijzend, Sofie M. Adriaanse, Wiesje M. Van der Flier, Charlotte E. Teunissen, Jan C. De Munck, Cornelis J. Stam, Philip Scheltens, Bart NM Van Berckel, Frederik Barkhof, and Alle Meije Wink. Brain network alterations in Alzheimer’s disease measured by eigenvector centrality in fMRI are related to cognition and CSF biomarkers. *Human brain mapping*, 35(5):2383–2393, 2014.
 - [72] Azzurra Invernizzi, Hinke N. Halbertsma, Martijn van Ackooij, Leonie Bais, Jeffrey Boertien, Remco J. Renken, Frans W. Cornelissen, and Teus van Laar. rTMS treatment of visual hallucinations using a connectivity-based targeting method - A case study. *Brain Stimulation: Basic, Translational, and Clinical Research in Neuromodulation*, 12(6):1622–1624, November 2019.
 - [73] Karl Pearson. VII. Note on regression and inheritance in the case of two parents. *proceedings of the royal society of London*, 58(347-352):240–242, 1895.
 - [74] Jacob Cohen. Statistical power analysis for the behavioral sciences. Abingdon. England: Routledge, 1988.
 - [75] Monika A. Myszczynska, Poojitha N. Ojamies, Alix M. B. Lacoste, Daniel Neil, Amir Saffari, Richard Mead, Guillaume M. Hautbergue, Joanna D. Holbrook, and Laura Ferraiuolo. Applications of machine learning to diagnosis and treatment of neurodegenerative diseases. *Nature Reviews Neurology*, 16(8):440–456, August 2020.
 - [76] V. Vapnik and A. Chervonenkis. On a class of algorithms of learning pattern recognition. *Automation and Remote Control*, 25:937–945, 1964.
 - [77] Bernhard E. Boser, Isabelle M. Guyon, and Vladimir N. Vapnik. A training algorithm for optimal margin classifiers. In *Proceedings of the Fifth Annual Workshop on Computational Learning Theory*, pages 144–152, 1992.
 - [78] Derek A. Pisner and David M. Schnyer. Chapter 6 - Support vector machine. In Andrea Mechelli and Sandra Vieira, editors, *Machine Learning*, pages 101–121. Academic Press, January 2020.
 - [79] S. R. Kay, A. Fiszbein, and L. A. Opler. The positive and negative syndrome scale (PANSS) for schizophrenia. *Schizophrenia Bulletin*, 13(2):261–276, 1987.

Chapter 6. Bibliography

- [80] Susan L. Rossell, Maya J. L. Schutte, Wei Lin Toh, Neil Thomas, Clara Strauss, Mascha M. J. Linszen, Edwin van Dellen, Sophie M. Heringa, Rob Teunisse, Christina W. Slotema, and Iris E. C. Sommer. The Questionnaire for Psychotic Experiences: An Examination of the Validity and Reliability. *Schizophrenia Bulletin*, 45(45 Suppl 1):S78–S87, February 2019.
- [81] Robert W. Cox, John Ashburner, Hester Breman, Kate Fissell, Christian Haselgrove, Colin J. Holmes, Jack L. Lancaster, David E. Rex, Stephen M. Smith, and Jeffrey B. Woodward. A (sort of) new image data format standard: NiFTI-1. In *10th Annual Meeting of the Organization for Human Brain Mapping*, volume 22, page 01, 2004.
- [82] Xiangrui Li, Paul S. Morgan, John Ashburner, Jolinda Smith, and Christopher Rorden. The first step for neuroimaging data analysis: DICOM to NIfTI conversion. *Journal of neuroscience methods*, 264:47–56, 2016.
- [83] Krzysztof J. Gorgolewski, Tibor Auer, Vince D. Calhoun, R. Cameron Craddock, Samir Das, Eugene P. Duff, Guillaume Flandin, Satrajit S. Ghosh, Tristan Glatard, Yaroslav O. Halchenko, Daniel A. Handwerker, Michael Hanke, David Keator, Xiangrui Li, Zachary Michael, Camille Maumet, B. Nolan Nichols, Thomas E. Nichols, John Pellman, Jean-Baptiste Poline, Ariel Rokem, Gunnar Schaefer, Vanessa Sochat, William Triplett, Jessica A. Turner, Gaël Varoquaux, and Russell A. Poldrack. The brain imaging data structure, a format for organizing and describing outputs of neuroimaging experiments. *Scientific Data*, 3(1):160044, June 2016.
- [84] Agah Karakuzu, Stefan Appelhoff, Tibor Auer, Mathieu Boudreau, Franklin Feingold, Ali R. Khan, Alberto Lazari, Chris Markiewicz, Martijn Mulder, Christophe Phillips, Taylor Salo, Nikola Stikov, Kirstie Whitaker, and Gilles de Hollander. qMRI-BIDS: An extension to the brain imaging data structure for quantitative magnetic resonance imaging data. *Scientific Data*, 9(1):517, August 2022.
- [85] Craddock Cameron, Sikka Sharad, Cheung Brian, Khanuja Ranjeet, Ghosh Satrajit, Yan Chaogan, Li Qingyang, Lurie Daniel, Vogelstein Joshua, Burns Randal, Colcombe Stanley, Mennes Maarten, Kelly Clare, Di Martino Adriana, Castellanos Francisco, and Milham Michael. Towards Automated Analysis of Connectomes: The Configurable Pipeline for the Analysis of Connectomes (C-PAC). *Frontiers in Neuroinformatics*, 7, 2013.
- [86] Mark Jenkinson, Christian F. Beckmann, Timothy E. J. Behrens, Mark W. Woolrich, and Stephen M. Smith. FSL. *NeuroImage*, 62(2):782–790, August 2012.
- [87] Bruce Fischl. FreeSurfer. *Neuroimage*, 62(2):774–781, 2012.
- [88] R. W. Cox. AFNI: Programvare for analyse og visualisering av funksjonell magnetisk resonans Neuroimages. *Comput Biomed Res*, 29:162–173, 1996.

Chapter 6. Bibliography

- [89] Robert W. Cox and James S. Hyde. Software tools for analysis and visualization of fMRI data. *NMR in Biomedicine: An International Journal Devoted to the Development and Application of Magnetic Resonance In Vivo*, 10(4-5):171–178, 1997.
- [90] Xin Yang, Paul T. Schrader, and Ning Zhang. A deep neural network study of the ABIDE repository on autism spectrum classification. *International Journal of Advanced Computer Science and Applications*, 11(4), 2020.
- [91] Alan C. Evans, Andrew L. Janke, D. Louis Collins, and Sylvain Baillet. Brain templates and atlases. *NeuroImage*, 62(2):911–922, August 2012.
- [92] Yongyue Zhang, Michael Brady, and Stephen Smith. Segmentation of brain MR images through a hidden Markov random field model and the expectation-maximization algorithm. *IEEE transactions on medical imaging*, 20(1):45–57, 2001.
- [93] Terrence R. Oakes, Tom Johnstone, KS Ores Walsh, Lawrence L. Greischar, Andrew L. Alexander, Andrew S. Fox, and Richard J. Davidson. Comparison of fMRI motion correction software tools. *Neuroimage*, 28(3):529–543, 2005.
- [94] William R. Shirer, Heidi Jiang, Collin M. Price, Bernard Ng, and Michael D. Greicius. Optimization of rs-fMRI Pre-processing for Enhanced Signal-Noise Separation, Test-Retest Reliability, and Group Discrimination. *NeuroImage*, 117:67–79, August 2015.
- [95] Dan Pan, An Zeng, Longfei Jia, Yin Huang, Tory Frizzell, and Xiaowei Song. Early Detection of Alzheimer’s Disease Using Magnetic Resonance Imaging: A Novel Approach Combining Convolutional Neural Networks and Ensemble Learning. *Frontiers in Neuroscience*, 14, 2020.
- [96] Alle Meije Wink. fastECM. <https://github.com/amwink/bias/>, 2012.
- [97] BrainHackDonostia. MNI152 mask. <https://git.bcbi.eu/brainhackdonostia/{\}/material-2019/tree/2fd574bb4340651ed6e853e88d551db9d6b1ee44/fMRI/{\}/fmriprep/templates>, 2019.
- [98] Jean-Philippe Fortin. MNI152 Template. <https://github.com/Jfortin1/MNITemplate>, 2020.
- [99] Alexandre Abraham, Fabian Pedregosa, Michael Eickenberg, Philippe Gervais, Andreas Mueller, Jean Kossaifi, Alexandre Gramfort, Bertrand Thirion, and Gaël Varoquaux. Machine learning for neuroimaging with scikit-learn. *Frontiers in neuroinformatics*, page 14, 2014.
- [100] Fabian Pedregosa, Gaël Varoquaux, Alexandre Gramfort, Vincent Michel, Bertrand Thirion, Olivier Grisel, Mathieu Blondel, Peter Prettenhofer, Ron Weiss, and Vincent Dubourg. Scikit-learn: Machine learning in Python. *the Journal of machine Learning research*, 12:2825–2830, 2011.

Chapter 6. Bibliography

- [101] Chris Rorden, Hans-Otto Karnath, and Leonardo Bonilha. Improving lesion-symptom mapping. *Journal of cognitive neuroscience*, 19(7):1081–1088, 2007.
- [102] Linchuan Zhang, Baojuan Li, Huaning Wang, Liang Li, Qimei Liao, Yang Liu, Xianghong Bao, Wenlei Liu, Hong Yin, Hongbing Lu, and Qingrong Tan. Decreased middle temporal gyrus connectivity in the language network in schizophrenia patients with auditory verbal hallucinations. *Neuroscience Letters*, 653:177–182, July 2017.
- [103] Anna Alonso-Solís, Yolanda Vives-Gilabert, Eva Grasa, Maria J. Portella, Mireia Rabella, Rosa Blanca Sauras, Alexandra Roldán, Fidel Núñez-Marín, Beatriz Gómez-Ansón, Víctor Pérez, Enric Alvarez, and Iluminada Corripio. Resting-state functional connectivity alterations in the default network of schizophrenia patients with persistent auditory verbal hallucinations. *Schizophrenia Research*, 161(2):261–268, February 2015.
- [104] M. E. Kalaitzakis, L. M. Christian, L. B. Moran, M. B. Graeber, R. K. B. Pearce, and S. M. Gentleman. Dementia and visual hallucinations associated with limbic pathology in Parkinson’s disease. *Parkinsonism & Related Disorders*, 15(3):196–204, March 2009.
- [105] Paul Allen, Frank Larøi, Philip K. McGuire, and Andrè Aleman. The hallucinating brain: A review of structural and functional neuroimaging studies of hallucinations. *Neuroscience & Biobehavioral Reviews*, 32(1):175–191, January 2008.
- [106] D. A. Silbersweig, E. Stern, C. Frith, C. Cahill, A. Holmes, Sylke Grootoornk, J. Seaward, P. McKenna, S. E. Chua, L. Schnorr, T. Jones, and R. S. J. Frackowiak. A functional neuroanatomy of hallucinations in schizophrenia. *Nature*, 378(6553):176–179, November 1995.
- [107] Klaas E. Stephan, Karl J. Friston, and Chris D. Frith. Dysconnection in schizophrenia: From abnormal synaptic plasticity to failures of self-monitoring. *Schizophrenia bulletin*, 35(3):509–527, 2009.
- [108] André Schmidt, Vaibhav A. Diwadkar, Renata Smieskova, Fabienne Harrisberger, Undine E. Lang, Philip McGuire, Paolo Fusar-Poli, and Stefan Borgwardt. Approaching a network connectivity-driven classification of the psychosis continuum: A selective review and suggestions for future research. *Frontiers in human neuroscience*, 8:1047, 2015.
- [109] Stefan Haufe, Frank Meinecke, Kai Görgen, Sven Dähne, John-Dylan Haynes, Benjamin Blankertz, and Felix Bießmann. On the interpretation of weight vectors of linear models in multivariate neuroimaging. *NeuroImage*, 87:96–110, February 2014.
- [110] Lu Chen, Chunchao Xia, and Huaiqiang Sun. Recent advances of deep learning in psychiatric disorders. *Precision Clinical Medicine*, 3(3):202–213, 2020.

Chapter 6. Bibliography

- [111] Yuki Hashimoto, Yousuke Ogata, Manabu Honda, and Yuichi Yamashita. Deep Feature Extraction for Resting-State Functional MRI by Self-Supervised Learning and Application to Schizophrenia Diagnosis. *Frontiers in Neuroscience*, 15, 2021.
- [112] Junghoe Kim, Vince D. Calhoun, Eunsoo Shim, and Jong-Hwan Lee. Deep neural network with weight sparsity control and pre-training extracts hierarchical features and enhances classification performance: Evidence from whole-brain resting-state functional connectivity patterns of schizophrenia. *NeuroImage*, 124:127–146, January 2016.
- [113] Alexander Selvikvåg Lundervold and Arvid Lundervold. An overview of deep learning in medical imaging focusing on MRI. *Zeitschrift für Medizinische Physik*, 29(2):102–127, 2019.
- [114] Hiroyuki Yamaguchi, Yuki Hashimoto, Genichi Sugihara, Jun Miyata, Toshiya Murai, Hidehiko Takahashi, Manabu Honda, Akitoyo Hishimoto, and Yuichi Yamashita. Three-Dimensional Convolutional Autoencoder Extracts Features of Structural Brain Images With a “Diagnostic Label-Free” Approach: Application to Schizophrenia Datasets. *Frontiers in Neuroscience*, 15:652987, July 2021.
- [115] Ling-Li Zeng, Huaning Wang, Panpan Hu, Bo Yang, Weidan Pu, Hui Shen, Xingui Chen, Zhening Liu, Hong Yin, Qingrong Tan, Kai Wang, and Dewen Hu. Multi-Site Diagnostic Classification of Schizophrenia Using Discriminant Deep Learning with Functional Connectivity MRI. *eBioMedicine*, 30:74–85, 2018.
- [116] JinChi Zheng, XiaoLan Wei, JinYi Wang, HuaSong Lin, HongRun Pan, and YuQing Shi. Diagnosis of Schizophrenia Based on Deep Learning Using fMRI. *Computational and Mathematical Methods in Medicine*, 2021:e8437260, November 2021.
- [117] Usman Mahmood, Md Mahfuzur Rahman, Alex Fedorov, Zening Fu, and Sergey Plis. Transfer Learning of fMRI Dynamics, November 2019.
- [118] Sunil Vasu Kalmady, Animesh Kumar Paul, Janardhanan C. Narayanaswamy, Rimjhim Agrawal, Venkataram Shivakumar, Andrew J. Greenshaw, Serdar M. Dursun, Russell Greiner, Ganeshan Venkatasubramanian, and Y. C. Janardhan Reddy. Prediction of Obsessive-Compulsive Disorder: Importance of Neurobiology-Aided Feature Design and Cross-Diagnosis Transfer Learning. *Biological Psychiatry: Cognitive Neuroscience and Neuroimaging*, 7(7):735–746, July 2022.
- [119] Mukul Singh, Shrey Bansal, Sakshi Ahuja, Rahul Kumar Dubey, Bijaya Ketan Panigrahi, and Nilanjan Dey. Transfer learning-based ensemble support vector machine model for automated COVID-19 detection using lung computerized tomography scan data. *Medical & Biological Engineering & Computing*, 59(4):825–839, April 2021.

Chapter 6. Bibliography

- [120] Syed Moshfeq Salaken, Abbas Khosravi, Thanh Nguyen, and Saeid Nahavandi. Extreme learning machine based transfer learning algorithms: A survey. *Neurocomputing*, 267:516–524, December 2017.

Appendix

PSVH⁺ vs. PSVH⁻

Performance

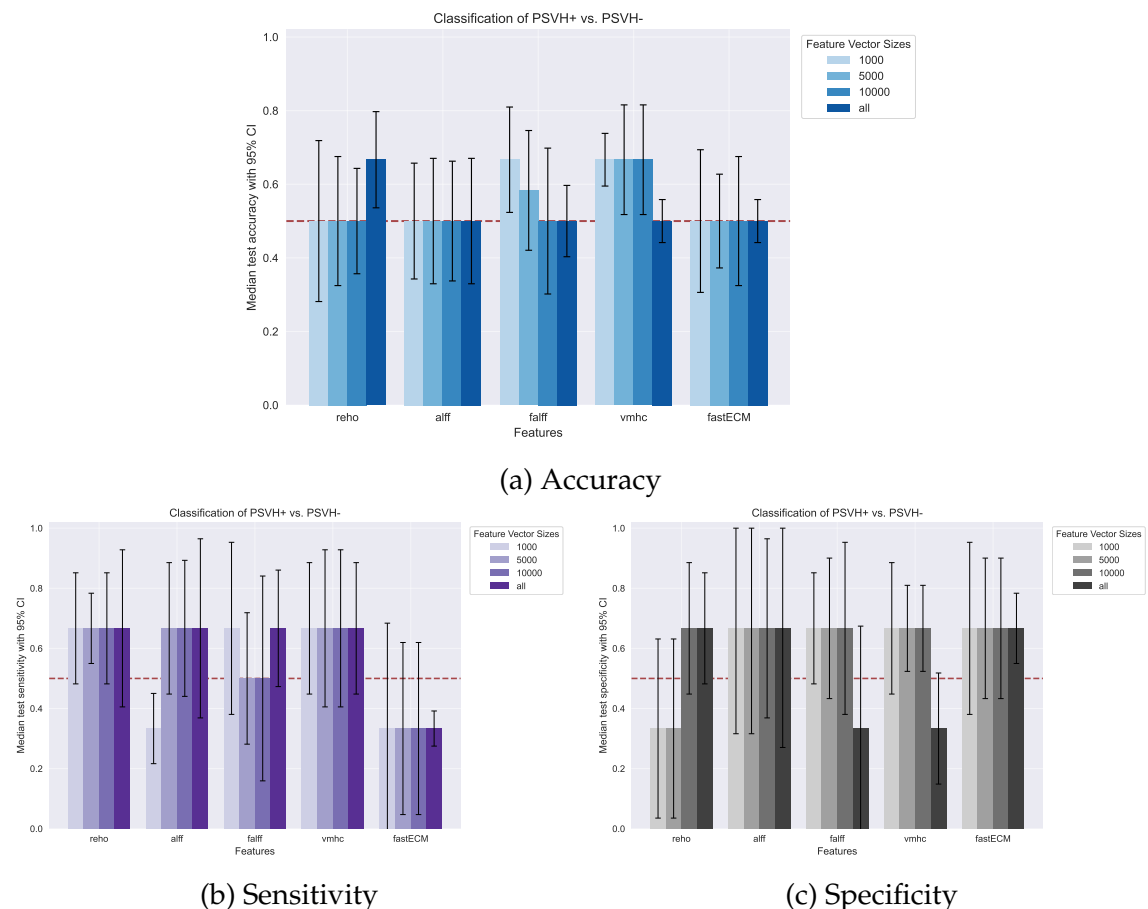


Figure 6.1: Median performance measures for the classification of PSVH⁺ vs. PSVH⁻ with 95% confidence intervals over five folds.

SVM weight maps

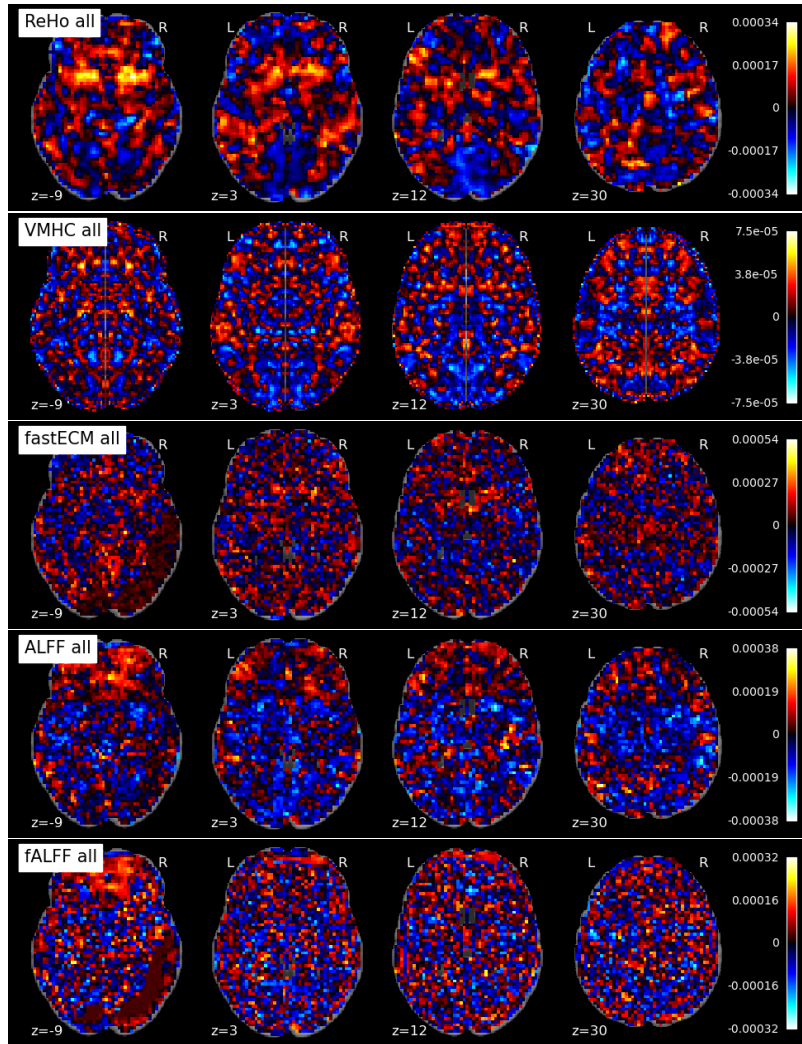


Figure 6.2: SVM weights for the classification of PSVH+ vs. PSVH- using ReHo, VMHC, fastECM, ALFF, and fALFF features (top to bottom) without feature selection.

Chapter 6. Bibliography

PSVH⁺ vs. HC

Performance

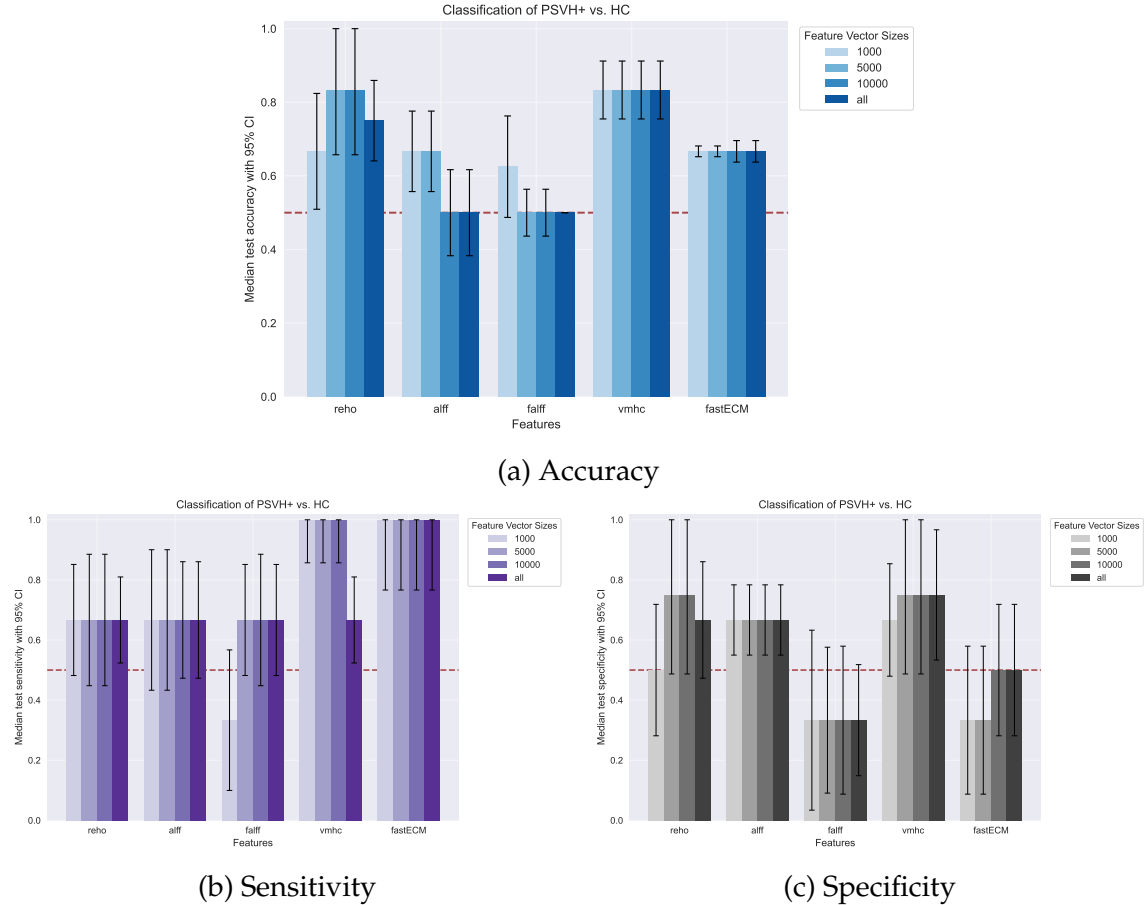


Figure 6.3: Median performance measures for the classification of PSVH⁺ vs. HC with 95% confidence intervals over five folds.

SVM weight maps

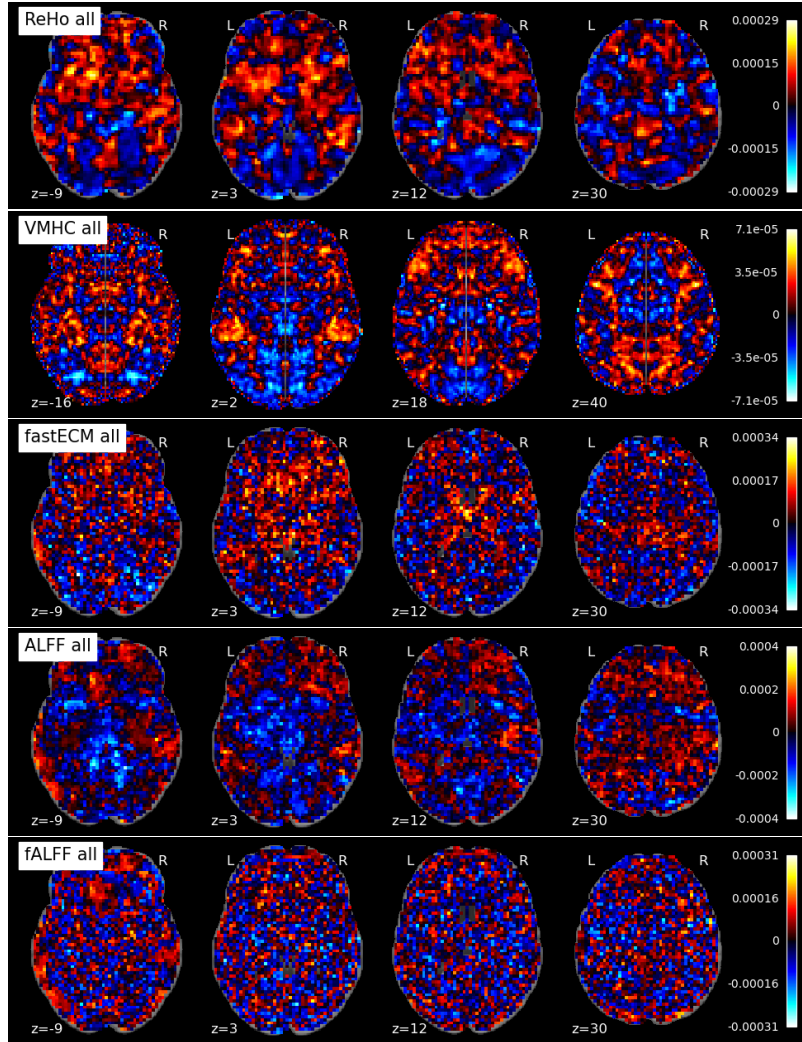


Figure 6.4: SVM weights for the classification of PSVH+ vs. HC using ReHo, VMHC, fastECM, ALFF, and fALFF features (top to bottom) without feature selection.

Chapter 6. Bibliography

PSVH⁻ vs. HC

Performance

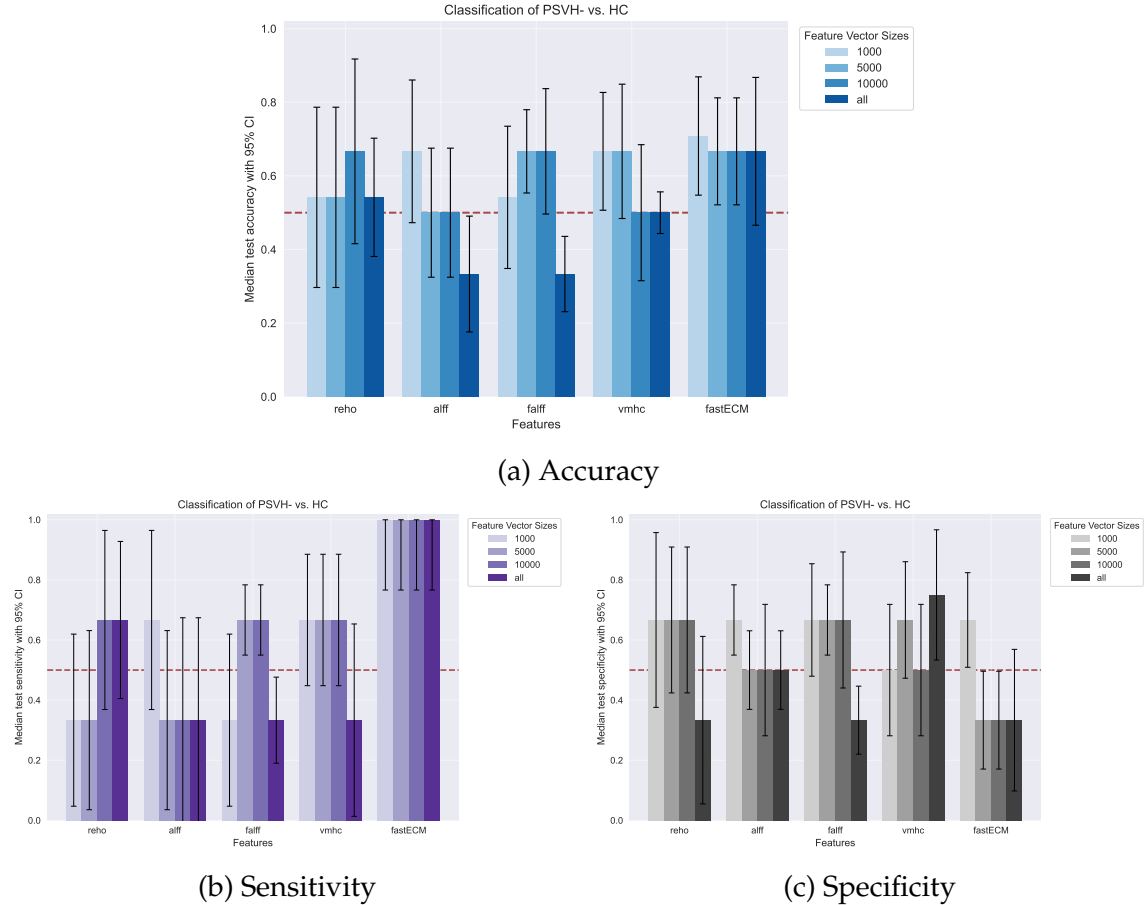


Figure 6.5: Median performance measures for the classification of PSVH⁻ vs. HC with 95% confidence intervals over five folds.

SVM weight maps

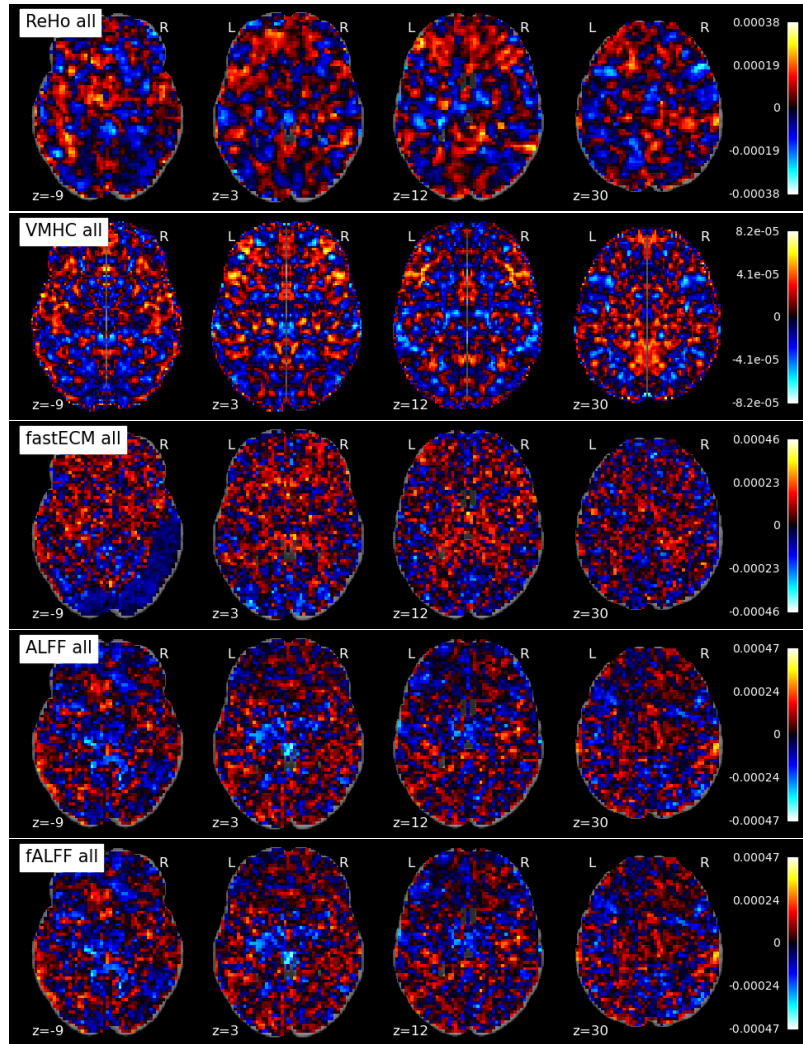


Figure 6.6: SVM weights for the classification of PSVH- vs. HC using ReHo, VMHC, fastECM, ALFF, and fALFF features (top to bottom) without feature selection.